

Quantum spin ice in three-dimensional Rydberg atom arrays

Jeet Shah,^{1,2} Gautam Nambiar,¹ Alexey V. Gorshkov,^{1,3} and Victor Galitski^{1,4}

¹*Joint Quantum Institute, Department of Physics,
University of Maryland, College Park, MD 20742, USA*

²*Condensed Matter Theory Center, Department of Physics,
University of Maryland, College Park, MD 20742, USA*

³*Joint Center for Quantum Information and Computer Science,
NIST/University of Maryland, College Park, MD 20742, USA*

⁴*Center for Computational Quantum Physics, The Flatiron Institute, New York, NY 10010, USA*

(Dated: January 13, 2023)

Quantum spin liquids are exotic phases of matter whose low-energy physics is described as the deconfined phase of an emergent gauge theory. With recent theory proposals and an experiment showing preliminary signs of \mathbb{Z}_2 topological order [G. Semeghini et al., *Science* **374**, 1242 (2021)], Rydberg atom arrays have emerged as a promising platform to realize a quantum spin liquid. In this work, we propose a way to realize a $U(1)$ quantum spin liquid in three spatial dimensions, described by the deconfined phase of $U(1)$ gauge theory in a pyrochlore lattice Rydberg atom array. We study the ground state phase diagram of the proposed Rydberg system as a function of experimentally relevant parameters. Within our calculation, we find that by tuning the Rabi frequency, one can access both the confinement-deconfinement transition driven by a proliferation of “magnetic” monopoles and the Higgs transition driven by a proliferation of “electric” charges of the emergent gauge theory. We suggest experimental probes for distinguishing the deconfined phase from ordered phases. This work serves as a proposal to access a confinement-deconfinement transition in three spatial dimensions on a Rydberg-based quantum simulator.

I. INTRODUCTION

When the classical part of a many-body Hamiltonian is frustrated, quantum fluctuations can break the degeneracy in interesting ways. An exotic form of such breaking was pointed out by Anderson [1] where the ground state is a superposition of several almost-degenerate states, and the excitations are “fractional” [2]. Broadly, a common feature tying together such systems called quantum spin liquids is that, at low energies, they can be described as lying in a deconfined phase of an emergent gauge theory. The fractional excitations are the “charge”-like and “flux/monopole”-like excitations of this gauge theory. When these fractional excitations get confined, they cease to be important for the low-energy physics, and the system becomes ordered. From this point of view, transitions from a spin liquid to conventional ordered phases are understood as a confinement-deconfinement transition, driven by a proliferation of “flux/monopole”-like excitations, or a Higgs transition, driven by a proliferation of “charge”-like excitations [3–6]. Gauge theories and their phase transitions are of fundamental importance in physics [7–10]. The prospect of this physics emerging in many-body systems provides an important motivation for studying quantum spin liquids. They are also interesting due to their possible role in the physics of strongly correlated materials [11] and possible application in quantum computing [12, 13].

Traditionally, the main search space for spin liquids has comprised of solid state systems. While consistent progress has been made [2, 14], conclusive evidence for spin liquids is still lacking in these systems. One reason is that the same feature that makes spin liq-

uids interesting—being characterized by non-local order parameters—also makes them hard to detect. Meanwhile, over the past decade, Rydberg atom arrays have emerged as a promising platform for engineering interacting Hamiltonians [15–36]. Rydberg states have large principal quantum number n ($\sim 20 - 100$), and the van der Waals interaction between them scales as n^{11} . The strong tunable interactions, along with the ability to customize the lattice of atoms, locally control qubits, and take wavefunction snapshots, make Rydberg atom arrays a competitive platform to explore quantum many-body physics. Following theory proposals [37, 38], promising signs of \mathbb{Z}_2 topological order have been observed experimentally on this platform [26]. This has sparked a lot of activity over the past two years in the general direction of proposing ways to realize exotic states on quantum devices using analogue quantum simulation [39–42], digital quantum simulation [43], and projective measurements [44, 45].

Our work is a proposal for realizing a $U(1)$ quantum spin liquid, described by the deconfined phase of a compact $U(1)$ gauge theory on three-dimensional Rydberg atom arrays, with an eye towards accessing the confinement-deconfinement transition. It was shown by Polyakov [46, 47] that compact $U(1)$ gauge theory in 2+1 dimensions is always in the confined phase in the thermodynamic limit due to a proliferation of monopole events. Therefore we turn to 3+1 dimensions, where Polyakov argued [47] for the existence of both deconfined and confined phases separated by a transition driven by monopole excitations. The deconfined phase consists of gapless “photons”, gapped “monopoles” and gapped “charge” excitations. In the early 2000s, lattice models

of spins [48] and dimers [49] on corner-sharing polyhedra were constructed that were strongly argued to realize this phase—a $U(1)$ spin liquid, using perturbation theory, solvable limits [48] and later Quantum Monte Carlo simulations [50, 51]. Our work is based on a spin model with easy-axis antiferromagnetic interactions introduced by Hermele et al. [48] on the pyrochlore lattice consisting of corner-sharing tetrahedra (see Fig. 1). The classical Ising limit of this model is the widely studied classical spin ice [52–56], which has a large residual entropy at low temperatures similar to water-ice [57]. This is because the ground states form an exponentially degenerate set of states obeying the “ice rule” (see Sec. II). The quantum model in Ref. [48] has also been a subject of intense study in the context of pyrochlore materials like $\text{Yb}_2\text{Ti}_2\text{O}_7$ and $\text{Er}_2\text{Ti}_2\text{O}_7$ as potential quantum spin ice (another name for the $U(1)$ spin liquid) candidates [58].

It was observed in Ref. [59] that the Hamiltonian in Ref. [48] can be viewed as that of hard-core bosons hopping on an optical lattice with nearest-neighbor repulsion, thus extending its relevance to the cold atom setting. Ref. [60] studied a similar model of hard-core bosons *hopping* on a two-dimensional checkerboard lattice. In Ref. [60], the atom’s internal state was largely the ground state, but a dressing with Rydberg states was used to engineer interactions between atoms. Later, Ref. [61] showed that dimer models in two dimensions can be implemented on configurable Rydberg arrays—where the atoms themselves are stationary but can internally be either in a ground state or in a Rydberg state. In this setting, the atoms are driven with a laser (or a pair of lasers making a two-photon transition) that is detuned from the ground to Rydberg transition. The Rydberg interactions and the detuning define a (frustrated) “classical” energy landscape. The laser driving induces quantum fluctuations controlled by the Rabi frequency, leading (perturbatively) to dimer moves or ring exchange terms that are required to deconfine a gauge theory. The proposal [37] and experiment [26] mentioned above worked in the same setting. Our work is also based on this setting in which the atom array is configured in a 3D pyrochlore lattice.

In Sec. II, we explain our proposal. We show that within a window of laser detunings, the classical landscape is identical to the set of ice rule obeying states. Our Hamiltonian, when restricted to nearest-neighbor interactions, is equivalent to the transverse-field Ising model on the pyrochlore lattice. In the limit of small Rabi frequencies, it is perturbatively equivalent to the model in [48], which was argued to have a spin liquid ground state. Away from the perturbative limit, there is numerical evidence for a spin liquid phase [62]. However, once we include the long-range $1/r^6$ interactions beyond nearest-neighbor, the classical landscape is no longer degenerate, and it is a priori unclear if the spin liquid survives as the ground state. We attempt to answer this in Sec. III by comparing the energy of an ansatz wave function of the spin liquid with that of an ordered state. Within our approximation, we find that by dialing up

the Rabi frequency, for fixed detuning and interaction strength, one goes through a confinement-deconfinement transition from an ice rule obeying ferromagnetic state into a deconfined spin liquid phase. Then, by further increasing the Rabi frequency, one goes through a Higgs transition from the spin liquid to a transverse-field-polarized state (see Sec. III B). While the analysis till this point focuses on the ground state, in Sec. III C, we comment on the role played by dynamical state-preparation in deciding the nature of the state prepared in experiment. In Sec. IV, we present correlation functions that distinguish the spin liquid from the confined phases, and provide experimental protocols for measuring them. Finally, in Sec. V, we present general discussions and conclusions.

II. PROPOSAL TO REALIZE A $U(1)$ QUANTUM SPIN LIQUID USING RYDBERG ATOMS

In this section, we describe our proposal to realize a $U(1)$ Quantum Spin Liquid (QSL) in Rydberg atom arrays. Consider a 3D Rydberg array in which the atoms are positioned on the sites of the pyrochlore lattice [see Fig. 1(a)]. Each of the atoms can either be in the ground state $|g\rangle$ or in the Rydberg state $|r\rangle$. In the rotating wave approximation and in a rotating frame, the Hamiltonian is

$$\hat{H}_{\text{ryd}} = -\delta \sum_i \hat{n}_i + \frac{V}{2} \sum_{i \neq j} \left(\frac{a}{|\mathbf{x}_i - \mathbf{x}_j|} \right)^6 \hat{n}_i \hat{n}_j + \frac{\Omega}{2} \sum_i (\hat{b}_i + \hat{b}_i^\dagger), \quad (1)$$

where $\hat{b}_i = |g_i\rangle \langle r_i|$, $\hat{n}_i = \hat{b}_i^\dagger \hat{b}_i$, Ω is the Rabi frequency, δ is the laser detuning, V is the nearest-neighbor van der Waals interaction strength, and a is the distance between two neighboring atoms. The summation $\sum_{i \neq j}$ is over distinct sites i and j of the pyrochlore lattice (each pair is being counted twice), and \sum_i is over sites i . Below, we briefly describe the pyrochlore lattice.

The pyrochlore lattice is a face-centred cubic (FCC) lattice with a four-site basis formed by the four vertices of an up-pointing tetrahedron. (Since each lattice site belongs to one up-pointing tetrahedron and one down-pointing tetrahedron, the down-pointing tetrahedra are formed automatically once we create the up-pointing tetrahedra.) In Cartesian coordinates, the primitive vectors of the FCC lattice are

$$\begin{aligned} \mathbf{a}_1 &= \sqrt{2}a(0, 1, 1), \\ \mathbf{a}_2 &= \sqrt{2}a(1, 0, 1), \\ \mathbf{a}_3 &= \sqrt{2}a(1, 1, 0). \end{aligned} \quad (2)$$

The pyrochlore lattice sites are physically located at $\mathbf{r} + \mathbf{e}_\mu/2$ [and labeled (\mathbf{r}, μ)], where \mathbf{r} is an FCC lattice

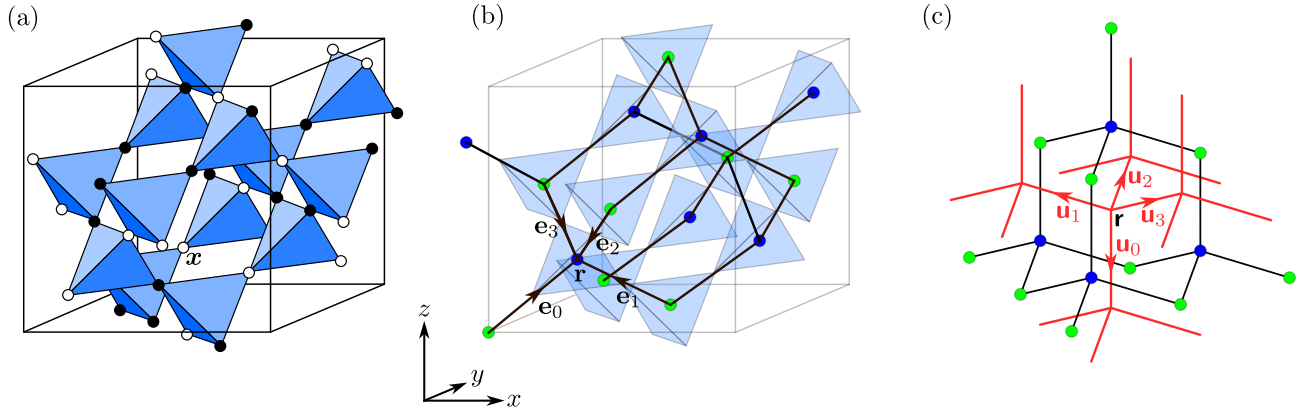


Figure 1: (a) The pyrochlore lattice. White circles denote atoms in the ground state, while black circles denote atoms in the Rydberg state. The configuration shown satisfies $n_{\Delta} = 2$ on each tetrahedron. The label \mathbf{x} is used to denote the sites of the pyrochlore lattice. (b) The diamond lattice. It is the bipartite lattice formed by the centers of the tetrahedra marked by green (A sublattice) and blue (B sublattice) dots. \mathbf{e}_μ for $\mu \in \{0, 1, 2, 3\}$ label the vectors joining an A site to its neighboring B sites. The label \mathbf{r} is used to denote the sites of the diamond lattice. (c) The red links are the edges of the lattice dual to the diamond lattice shown in (b). This lattice is also a diamond lattice, and we refer to it as the “dual diamond lattice” in this paper to distinguish it from the “diamond lattice” in (b). The sites of the dual diamond lattice are centers of the “polyhedra” formed by four puckered hexagons of the diamond lattice. \mathbf{u}_μ for $\mu \in \{0, 1, 2, 3\}$ label the vectors joining an A site to its neighboring B sites on the dual diamond lattice. The label \mathbf{r} [notice the difference in the font as compared to \mathbf{r} in (b)] is used to denote the sites of the dual diamond lattice.

vector, and the vectors \mathbf{e}_μ for $\mu \in \{0, 1, 2, 3\}$ are defined as [see Fig. 1(b)]

$$\begin{aligned} \mathbf{e}_0 &= \frac{a}{\sqrt{2}}(1, 1, 1) = \frac{1}{4}(\mathbf{a}_1 + \mathbf{a}_2 + \mathbf{a}_3), \\ \mathbf{e}_1 &= \frac{a}{\sqrt{2}}(1, -1, -1), \\ \mathbf{e}_2 &= \frac{a}{\sqrt{2}}(-1, 1, -1), \\ \mathbf{e}_3 &= \frac{a}{\sqrt{2}}(-1, -1, 1). \end{aligned} \quad (3)$$

We map the two levels of the atoms to spins-1/2s: $|g\rangle \rightarrow |\downarrow\rangle$, $|r\rangle \rightarrow |\uparrow\rangle$, $\hat{n}_i \rightarrow \hat{S}_i^z + 1/2$ and $\hat{b}_i + \hat{b}_i^\dagger \rightarrow 2\hat{S}_i^x$. The term $\hat{n}_i \hat{n}_j$ therefore maps to an $\hat{S}_i^z \hat{S}_j^z$ interaction in addition to a Zeeman term \hat{S}_i^z . Written in terms of spins, the Hamiltonian, up to an additive constant, is

$$\begin{aligned} \hat{H}_{\text{ryd}} &= -h \sum_i \hat{S}_i^z + \frac{V}{2} \sum_{i \neq j} \left(\frac{a}{|\mathbf{x}_i - \mathbf{x}_j|} \right)^6 \hat{S}_i^z \hat{S}_j^z \\ &\quad + \Omega \sum_i \hat{S}_i^x, \end{aligned} \quad (4)$$

where

$$h = \delta - \frac{V}{2} \sum_{i \neq 0} \left(\frac{a}{|\mathbf{x}_i - \mathbf{x}_0|} \right)^6, \quad (5)$$

and is independent of the choice of \mathbf{x}_0 for an infinite lattice. Evaluating this sum numerically for the pyrochlore lattice, we obtain $h = \delta - 3.46V$. It is useful to separate the total Hamiltonian, Eq. (4), into three parts,

$$\hat{H}_{\text{ryd}} = \hat{H}_0 + \hat{H}_\Omega + \hat{H}_{\text{LR}}, \text{ where}$$

$$\begin{aligned} \hat{H}_0 &= \frac{V}{2} \sum_{\langle i, j \rangle} \hat{S}_i^z \hat{S}_j^z - h \sum_i \hat{S}_i^z, \\ \hat{H}_\Omega &= \Omega \sum_i \hat{S}_i^x, \text{ and } \hat{H}_{\text{LR}} = \frac{V}{2} \sum'_{i \neq j} \left(\frac{a}{|\mathbf{x}_i - \mathbf{x}_j|} \right)^6 \hat{S}_i^z \hat{S}_j^z, \end{aligned} \quad (6)$$

where $\sum_{\langle i, j \rangle}$ is over nearest-neighbor pairs and $\sum'_{i \neq j}$ in \hat{H}_{LR} is over the remaining pairs that are not nearest-neighbor (in both \sum and \sum' , each pair is counted twice). The coefficients of the second, third, and fourth nearest-neighbor interactions are $V/27$, $V/64$, and $V/125$, respectively. Since these are small in comparison to V , we will drop \hat{H}_{LR} for the rest of this section because doing so allows us to connect to some previously known results [48, 51, 63]. We will study the effect of the long-range van der Waals interaction \hat{H}_{LR} in Sec. III.

Since the pyrochlore lattice is made of corner-sharing tetrahedra and since all edges in a tetrahedron are of equal length, we see that \hat{H}_0 can be written up to an additive constant as (for convenience, in the expression below, we switch back to the hard-core boson notation)

$$\hat{H}_0 = \frac{V}{2} \sum_{\Delta_r} (\hat{n}_{\Delta_r} - \rho)^2, \quad (7)$$

where the sum is over all tetrahedra, $\rho = \frac{1}{2} (4 + \frac{h}{V}) = \frac{1}{2} (0.54 + \frac{\delta}{V})$, and $\hat{n}_{\Delta_r} = \sum_{i \in \Delta_r} \hat{n}_i$ denotes the total number of atoms in the excited state on a given tetrahedron Δ_r . Minimizing \hat{H}_0 to obtain the classical ground

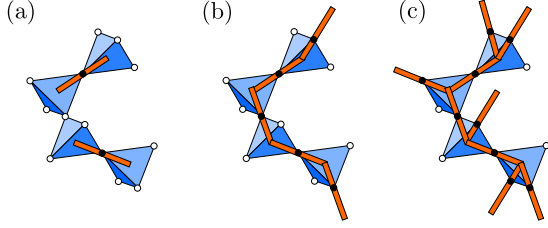


Figure 2: Mapping between Rydberg array configurations and dimer configurations. A Rydberg atom (black dot) is mapped to the presence of a dimer (orange bar), while a ground state atom (white dot) is mapped to the absence of a dimer. (a), (b), and (c) show example dimer configurations corresponding to $n_{\Delta} = 1, 2$, and 3 , respectively. In each case, n_{Δ} many dimers touch the center of each tetrahedron (the centers of the tetrahedra form the diamond lattice).

state imposes a constraint on n_{Δ} for each tetrahedron depending on the value of ρ :

$$n_{\Delta} = \begin{cases} 0 & \text{if } \rho < 1/2, \\ \text{floor}(\rho + \frac{1}{2}) & \text{if } 1/2 < \rho < 7/2, \\ 4 & \text{if } 7/2 < \rho. \end{cases} \quad (8)$$

The cases $n_{\Delta} = 0$ and $n_{\Delta} = 4$ are trivial, in that the classical ground state is unique. However, in the remaining cases, namely $n_{\Delta} = 1, 2, 3$, the classical ground state manifold is degenerate with exponentially (in system size) many states in it. In the case $n_{\Delta} = 2$, the number of configurations satisfying this constraint is approximately $(3/2)^{N_{\text{tetrahedra}}}$ (where $N_{\text{tetrahedra}}$ is the number of tetrahedra) [64]. This is based on an argument similar to the one given by Pauling to explain the residual entropy of water-ice at zero temperature [57]. From now onward, we will refer to the condition $n_{\Delta} = 2$ as the “ice rule”. An ice rule obeying configuration is shown in Fig. 1(a). In these non-trivial cases, the configurations with fixed n_{Δ} can be mapped to configurations of dimers on the bipartite diamond lattice formed by the centers of tetrahedra of the pyrochlore lattice [Fig. 1(b)], with exactly n_{Δ} many dimers touching each diamond site (see Fig. 2). The A and B sites of the diamond lattice are located at \mathbf{n} and $\mathbf{n} + \mathbf{e}_0$, respectively, where \mathbf{n} is an FCC lattice vector. For later use in this paper, we also show the lattice dual to this diamond lattice in Fig. 1(c) (also a diamond lattice, which we call the “dual diamond lattice”). An atom in the Rydberg state on site i is mapped to a dimer on the corresponding link of the diamond lattice, while an atom in the ground state is mapped to no dimer. Such dimer models have been studied extensively in both two and three dimensions [48, 65–67].

In the limit $\Omega \ll V$, \hat{H}_{Ω} leads to quantum fluctuations that break the exponential degeneracy of the low-energy manifold. We will study this effect perturbatively in the following section (Sec. II A). Classically, the energy gap between the degenerate ground state space

and the lowest excited states corresponding to two tetrahedra violating Eq. (8) by either $+1$ or -1 is $2V \times \min(\{\rho + 1/2\}, 1 - \{\rho + 1/2\})$. Here, $\{x\} \equiv x - \text{floor}(x)$ is the fractional part of x . It should be noted that, in the borderline cases when $\rho = m + 1/2$ with $m \in \{0, 1, 2, 3\}$, the energy gap closes and our perturbative analysis cannot be used. We assume going forward that ρ is away from these borderline values.

A. Perturbation theory

We work in the limit $\Omega \ll V$ and treat \hat{H}_{Ω} as a perturbation over \hat{H}_0 , ignoring for now \hat{H}_{LR} whose effects will be considered later in Sec. III. We calculate the effective Hamiltonian within the ground state manifold of \hat{H}_0 using the Schrieffer-Wolff formulation of perturbation theory. For simplicity, we present the calculation of the effective Hamiltonian only for $n_{\Delta} = 2$ here. The only difference between these three cases will be the Hilbert space on which the Hamiltonian acts. Calculating, at k^{th} order in perturbation theory, the matrix element of the effective Hamiltonian between two states $|n\rangle$ and $|m\rangle$ lying in the degenerate manifold involves starting from $|m\rangle$, applying the perturbation k times, and reaching the state $|n\rangle$. Since \hat{H}_{Ω} changes the particle number by ± 1 , the corrections at all odd orders are zero. Hence, we need to consider only the corrections at even orders.

Acting with $\frac{\Omega}{2}(\hat{b}_i + \hat{b}_i^{\dagger})$ on an ice rule obeying state creates two excited tetrahedra (whose common site is i), which violate the constraint $n_{\Delta} = 2$. Therefore, the only second-order process that takes us back to the ice manifold (the degenerate manifold of the ice rule obeying states) is the one in which two excited tetrahedra are created and annihilated, as illustrated in Figs. 3(a) and (b).

Since such processes are present for all the states of the ice manifold, they contribute only a constant energy shift and can be ignored. The same is true for the fourth-order processes. Now, the pyrochlore lattice has hexagonal plaquettes, some of which are shown in Fig. 4. This allows for non-trivial processes to exist at sixth order. In fact, non-trivial ring exchange over hexagonal plaquettes of the pyrochlore lattice is obtained by the process shown in Figs. 3(a)–(g) (some sixth-order processes also result in a constant energy shift which we neglect). A flippable configuration—one in which atoms on a hexagonal plaquette are alternately in the ground and Rydberg states—is mapped to the complementary flippable configuration by the ring exchange process as illustrated in Fig. 3(h). Thus, the effective Hamiltonian consists of ring exchange terms:

$$\hat{H}_{\text{eff}} = -J_{\text{ring}}(\rho) \sum_{\text{O}} |\text{O}\rangle \langle \text{O}| + \text{H.c.}, \quad (9)$$

where $J_{\text{ring}}(\rho) = \gamma(\rho)\Omega^6/V^5$, the sum is over all hexagonal plaquettes of the pyrochlore lattice, and $\gamma(\rho)$ is a

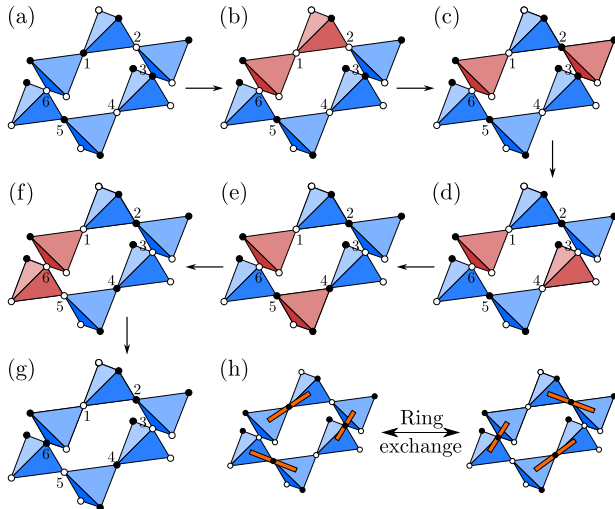


Figure 3: (a) and (b) constitute a virtual process at second order in perturbation theory in Ω/V . Starting from (a) which is a configuration that satisfies $n_{\Delta} = 2$ on all sites, $\hat{b}_1 + \hat{b}_1^\dagger$ is applied giving (b). To complete the second order process, $\hat{b}_1 + \hat{b}_1^\dagger$ is applied to (b) giving back (a). Sub-figures (a)–(g) constitute a sixth-order process in the perturbation theory that contributes to the ring exchange term in the effective Hamiltonian, Eq. (9). Starting from (a), the perturbation $\hat{b}_i + \hat{b}_i^\dagger$ is applied sequentially on sites $i = 1, 2, \dots, 6$. At the end of the six steps, a configuration with $n_{\Delta} = 2$ is obtained as shown in (g). Note that the configuration of the atoms on the hexagon is flipped in (g) as compared to (a) thereby producing the effect of a ring exchange. Other sixth-order processes where the perturbation is not applied sequentially also contribute to Eq. (9), but are not shown here. (h) Ring exchange process which appears in the effective Hamiltonian Eq. (9). A flippable configuration is mapped to the complimentary flippable configuration.

dimensionless number obtained by summing over virtual processes and is plotted as a function of ρ in Fig. 5. We note that, when ρ is an integer, the value of $\gamma(\rho)$ is $63/16$ and is the same as the one appearing in Refs. [68, 69]. Although the effective Hamiltonian was derived here assuming $n_{\Delta} = 2$, the effective Hamiltonian we obtain for $n_{\Delta} = 1, 3$ is also given by Eq. (9).

In terms of dimers on the diamond lattice, the effective Hamiltonian Eq. (9) corresponds to a kinetic energy of the dimers. It is well known that dimer models can be made exactly solvable by adding a potential energy V_{RK} for the dimers and tuning to a special point $V_{RK} = J_{\text{ring}}$ called the Rokhsar-Kivelson (RK) point [65]. The Hamil-

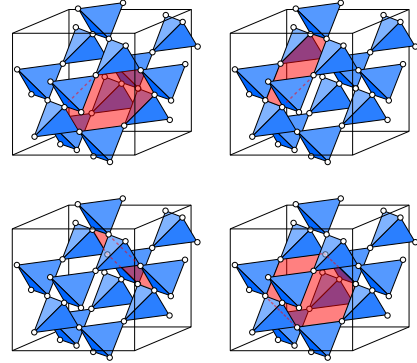


Figure 4: Shaded in red are the four nonequivalent hexagonal plaquettes of the pyrochlore lattice.

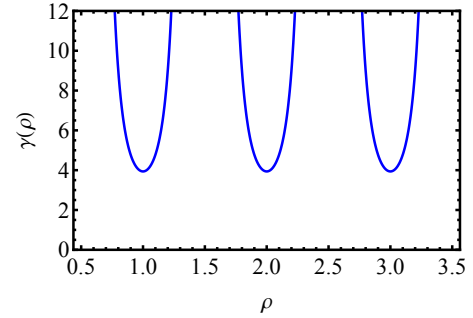


Figure 5: Plot showing the variation of $\gamma(\rho)$ (which is the proportionality constant in $J_{\text{ring}}(\rho) = \gamma(\rho)\Omega^6/V^5$) as a function of ρ . For $\rho = 0.5, 1.5, 2.5$, and 3.5 , the energy gap between the low-energy and the high-energy sectors closes and $\gamma(\rho)$ diverges.

tonian with such a potential energy term takes the form

$$\begin{aligned} \hat{H}_{\text{dimer}} = & - J_{\text{ring}}(\rho) \sum_{\bigcirc} |\text{dimer}\rangle \langle \text{dimer}| + \text{H.c.} \quad (10) \\ & + V_{RK} \sum_{\bigcirc} |\text{dimer}\rangle \langle \text{dimer}| + |\text{dimer}\rangle \langle \text{dimer}|. \end{aligned}$$

The Rydberg system we are interested in [Eq. (9)] is obtained from Eq. (10) by setting $V_{RK} = 0$.

B. $U(1)$ quantum spin liquid—relation to Hermele-Fisher-Balents [48]

The Hamiltonian in Eq. (10) was also derived by Hermele, Fisher and Balents in Ref. [48] starting from the Heisenberg model on the pyrochlore lattice and taking the easy-axis limit where the Hamiltonian is

$$\hat{H}_{\text{easy-axis}} = \frac{1}{2} \sum_{\langle i,j \rangle} \left[J_z \hat{S}_i^z \hat{S}_j^z + J_{\perp} \left(\hat{S}_i^x \hat{S}_j^x + \hat{S}_i^y \hat{S}_j^y \right) \right], \quad (11)$$

where $J_z \gg J_{\perp} > 0$. When $J_{\perp} = 0$, the ground state is exponentially degenerate with $S_{\Delta}^z = 0$ on each tetrahedron, which is equivalent to $n_{\Delta} = 2$. The J_{\perp} term was

treated as a perturbation over the J_z term, and at third order, a ring exchange term identical to Eq. (9) was obtained. Written in terms of the spins, the ring-exchange term is

$$\hat{H}_{\text{eff}} = -J_{\text{ring}} \sum_{\bigcirc} \hat{S}_1^+ \hat{S}_2^- \hat{S}_3^+ \hat{S}_4^- \hat{S}_5^+ \hat{S}_6^- + \text{H.c.}, \quad (12)$$

where the sum is over hexagonal plaquettes of the pyrochlore lattice. The RK potential term was added by hand in Ref. [48] giving Eq. (10).

Hermele et al. then go to the quantum rotor variables $n_{\mathbf{r}\mathbf{r}'} \in \mathbb{Z}$ and $\theta_{\mathbf{r}\mathbf{r}'} \in [-\pi, \pi]$, which live on the links $\mathbf{r}\mathbf{r}'$ of the diamond lattice (equivalently, sites of the pyrochlore lattice) and satisfy the canonical commutation relations $[\hat{n}_{\mathbf{r}\mathbf{r}'}, \hat{\theta}_{\mathbf{r}\mathbf{r}'}] = i$:

$$\hat{S}^z \rightarrow \hat{n} - \frac{1}{2}, \quad \hat{S}^\pm \rightarrow e^{\pm i\hat{\theta}}. \quad (13)$$

The constraint $n = 0$ or 1 is imposed by adding a term to the Hamiltonian that energetically penalizes states violating this constraint:

$$\begin{aligned} \hat{H}_{\text{eff}} = & \frac{U}{2} \sum_{\langle \mathbf{r}, \mathbf{r}' \rangle} \left(\hat{n}_{\mathbf{r}\mathbf{r}'} - \frac{1}{2} \right)^2 \\ & - 2J_{\text{ring}} \sum_{\bigcirc} \cos(\hat{\theta}_1 - \hat{\theta}_2 + \hat{\theta}_3 - \hat{\theta}_4 + \hat{\theta}_5 - \hat{\theta}_6), \end{aligned} \quad (14)$$

where the first sum is over all the links of the diamond lattice and the second one is over the hexagonal plaquettes of the pyrochlore lattice. In the limit $U \rightarrow \infty$, Eq. (14) reduces to the effective Hamiltonian Eq. (12).

The local constraint, $S_{\Delta_r}^z = 0$ for each tetrahedron, gives a gauge structure to the effective Hamiltonian where the gauge transformations are generated by $\hat{S}_{\Delta_r}^z$. The presence of this local symmetry motivated Hermele et al. to write Eq. (14) as a lattice $U(1)$ gauge theory. The electric field and the vector potential were defined as

$$\hat{e}_{\mathbf{r}\mathbf{r}'} = \pm \left(\hat{n}_{\mathbf{r}\mathbf{r}'} - \frac{1}{2} \right), \quad \hat{a}_{\mathbf{r}\mathbf{r}'} = \pm \hat{\theta}_{\mathbf{r}\mathbf{r}'}. \quad (15)$$

The positive (negative) sign is chosen if \mathbf{r} belongs to A (B) sublattice of the diamond lattice. The Hamiltonian written in terms of the electric field and the vector potential takes the form of a compact $U(1)$ lattice gauge theory [46, 70]:

$$\hat{H}_{\text{eff}} = \frac{U}{2} \sum_{\langle \mathbf{r}, \mathbf{r}' \rangle} \hat{e}_{\mathbf{r}\mathbf{r}'}^2 - 2J_{\text{ring}} \sum_{\bigcirc} \cos((\text{curl } \hat{a})_{\bigcirc}), \quad (16)$$

where the second summation is over hexagonal plaquettes of the diamond lattice and

$$(\text{curl } \hat{a})_{\bigcirc} = \sum_{\mathbf{r}, \mathbf{r}' \in \bigcirc} \hat{a}_{\mathbf{r}\mathbf{r}'}, \quad (17)$$

where $\sum_{\mathbf{r}, \mathbf{r}' \in \bigcirc}$ is a sum along the directed bonds of a hexagonal plaquette of the diamond lattice. The adjective “compact” refers to the vector potential $\hat{a}_{\mathbf{r}\mathbf{r}'}$ being an angular variable. There is an important difference between the above gauge theory and the compact $U(1)$ gauge theory studied by Polyakov [46, 47, 71]—the gauge theory obtained by Hermele et al. is an odd gauge theory, i.e., electric fields are half-integers, $e_{\mathbf{r}\mathbf{r}'} \in \mathbb{Z} + 1/2$, while the gauge theory studied by Polyakov was an even gauge theory, i.e., the electric fields were integers, $e_{\mathbf{r}\mathbf{r}'} \in \mathbb{Z}$. Because of this difference, the phases of the two theories differ.

The phases of a gauge theory can be characterized by the interaction between two externally added opposite electric charges separated by a distance R . If the potential between charges goes to zero (or increases as at most $\log R$ in 2+1D) as $R \rightarrow \infty$, then the gauge theory is in the deconfined phase. On the other hand, if the potential increases linearly with R or faster, then these opposite charges cannot be separated, and the gauge theory is in the confined phase. In the limit $U \rightarrow \infty$, the even gauge theory was shown to be in the confined phase in Refs. [46, 70], while the odd gauge theory can be in either the confined phase or the deconfined phase [48]. This can be understood intuitively as follows.

In the even gauge theory, in the limit $U \rightarrow \infty$, the electric fields are forced to be 0, $e_{\mathbf{r}\mathbf{r}'} = 0$, to minimize the energy in the absence of any external charges. However, in the presence of two opposite external charges, the Gauss's law requires that the electric field can no longer be zero everywhere. The spreading of the electric field is, however, penalized by the term $\frac{U}{2} \sum_{\langle \mathbf{r}, \mathbf{r}' \rangle} \hat{e}_{\mathbf{r}\mathbf{r}'}^2$. This forces the electric field to be nonzero only in a narrow tube joining the two charges, leading to a linearly rising potential between the two charges. Thus, in the limit $U \rightarrow \infty$, the even gauge theory is in a confined phase, and there is no deconfined phase in this limit. This confinement of charges has been shown in Refs. [46, 47, 70, 72].

On the other hand, in an odd gauge theory, in the limit $U \rightarrow \infty$, the electric field can take two values, $e_{\mathbf{r}\mathbf{r}'} = \pm 1/2$. This results in frustration, i.e., allows for many configurations of the electric field, so that the ground state in this limit is non-trivial. When two external charges are introduced, the electric field is not necessarily confined in a string between the charges, but can spread in space similar to the familiar Coulomb-law field lines of a non-compact $U(1)$ gauge theory. This suggests that it is possible for the odd gauge theory to be in the deconfined phase even in the $U \rightarrow \infty$ limit. In fact, the odd gauge theory on the pyrochlore lattice (14) is indeed in the deconfined phase in the $U \rightarrow \infty$ limit [50, 51, 63].

Hermele et al. have shown that the dimer model with the Hamiltonian Eq. (10) is described by the deconfined phase of the underlying compact $U(1)$ gauge theory close to the RK point (for V_{RK} smaller than J_{ring} but close to J_{ring}). This phase is the $U(1)$ quantum spin liquid. It has three types of emergent excitations—gapless photons, gapped magnetic monopoles and gapped fractional-

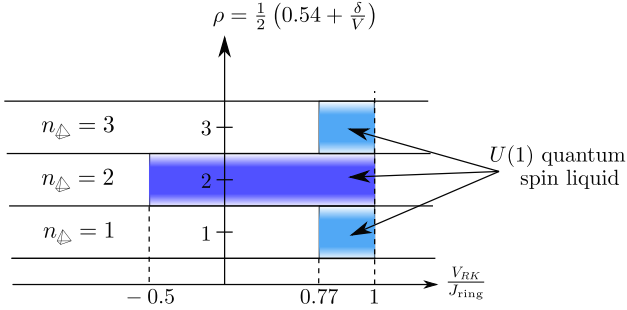


Figure 6: For $\rho \in (3/2, 5/2)$, corresponding to $n_{\Delta} = 2$, the system is in the $U(1)$ spin liquid phase at $V_{RK} = 0$ [51]. On the other hand, for $\rho \in (1/2, 3/2)$ and $\rho \in (5/2, 7/2)$, corresponding to $n_{\Delta} = 1$ and 3, respectively, the system is in an ordered phase at $V_{RK} = 0$ [63]. Note that for $\rho = 1/2, 3/2$, and $5/2$, the perturbation theory described in Sec. II A does not apply, and we cannot comment on the phase of the system.

ized electric charges, also called as spinons. The spinons are the tetrahedra which violate the constraint on n_{Δ} , Eq. (8).

C. Previous numerical work

In this section, we summarize some of the known work on the dimer model with the Hamiltonian Eq. (10) and on the nearest-neighbor transverse-field Ising model on the pyrochlore lattice.

Using quantum Monte Carlo simulations, Refs. [51] and [63] studied the range of V_{RK} [see Eq. (10)] over which the $U(1)$ spin liquid exists. They found that the spin liquid is present in the range $-0.5J_{\text{ring}} < V_{RK} < J_{\text{ring}}$ for the dimer model with $n_{\Delta} = 2$ and in the range $0.77J_{\text{ring}} < V_{RK} < J_{\text{ring}}$ for the dimer model with $n_{\Delta} = 1$. The dimer model with $n_{\Delta} = 3$ is equivalent to the one with $n_{\Delta} = 1$ by a particle-hole transformation. These numerical results are summarized in Fig. 6.

While a theory proposal to realize the RK potential exists [73], the RK potential is a six-body term for the pyrochlore lattice and is difficult to engineer experimentally. Thus, we focus on the case where $V_{RK} = 0$. From Fig. 6, we see that to obtain a spin liquid phase for $V_{RK} = 0$, one must have $n_{\Delta} = 2$, which corresponds to $3/2 < \rho < 5/2$. In the cases $n_{\Delta} = 1$ and 3, the system is in an ordered state when $V_{RK} = 0$. Hence, in conclusion, assuming the long-range interactions \hat{H}_{LR} can be ignored, we expect that, in the limit $\Omega \ll V$, the Rydberg system will be in a $U(1)$ quantum spin liquid phase for $3/2 < \rho < 5/2$.

When $\rho = 2$, or equivalently $h = 0$, and the long-range interactions \hat{H}_{LR} are ignored, the Hamiltonian of the system $\hat{H}_0 + \hat{H}_{\Omega}$ in Eq. (6) is the transverse field Ising model on the pyrochlore lattice. For $\Omega \ll V$, we know from the perturbative analysis of Sec. II A and Ref. [63] that the system is in the $U(1)$ quantum spin liquid phase.

For large Ω/V , where perturbation theory cannot be applied, Ref. [62] found using quantum Monte Carlo calculations that the $U(1)$ spin liquid exists in the region $\Omega < 0.55(5)V$, while, for $\Omega > 0.55(5)V$, the system is in a transverse-field-polarized (TFP) phase, which extends to $\Omega/V \rightarrow \infty$ where the ground state is polarized in the x -direction. This transition was also studied in Ref. [74] using perturbation theory, where a transition was found at $\Omega \approx 0.6V$.

The effects of adding a third nearest-neighbor interaction, V_{3NN} , to the dimer model were considered in Ref. [75]. It was found that the quantum spin liquid transitioned into an ordered state (antiferromagnet [76]) at $V_{3NN} \approx J_{\text{ring}}$. Thus non-nearest-neighbor interactions can destabilize the quantum spin liquid. In fact, in a 2D model with neutral atoms located on the bonds of a kagome lattice (same as the sites of a ruby lattice), a spin liquid ground state was found if the interactions were short-ranged using DMRG on cylinders [26, 37]. However, with the full long-range van der Waals interactions, the spin liquid ceased to exist [26, 37]. Thus it is important to consider the effects of long-range interactions. In the following section, we will study the phase diagram of Hamiltonian (6) in the presence of long-range interactions, using approximate methods.

III. PHASE DIAGRAM—APPROXIMATE METHODS

The goal of this section is to study the ground state phase diagram of Hamiltonian (4) for $\delta = 3.46V$ (which corresponds to $\rho = 2$) including long-range interactions \hat{H}_{LR} .

A. Confinement-deconfinement transition—Monte Carlo assisted perturbation theory

Consider the full Hamiltonian $\hat{H} = \hat{H}_0 + \hat{H}_{\Omega} + \hat{H}_{LR}$ from Eq. (6) in the case $\rho = 2$ [see Eq. (7)]:

$$\begin{aligned} \hat{H}_0 &= \frac{V}{2} \sum_{\Delta_r} \left(\sum_{i \in \Delta_r} \hat{S}_i^z \right)^2, \\ \hat{H}_{\Omega} &= \Omega \sum_i \hat{S}_i^x, \text{ and } \hat{H}_{LR} = \frac{V}{2} \sum_{i \neq j}' \left(\frac{a}{|\mathbf{x}_i - \mathbf{x}_j|} \right)^6 \hat{S}_i^z \hat{S}_j^z. \end{aligned} \quad (18)$$

The long-range interaction \hat{H}_{LR} splits the exponential degeneracy of the ice manifold, and selects one configuration diagonal in the \hat{S}^z basis as the ground state of $\hat{H}_0 + \hat{H}_{LR}$, which we call the “ordered state”. On the other hand, \hat{H}_{Ω} prefers superpositions of ice rule obeying states, the $U(1)$ quantum spin liquid (QSL) being one such superposition. Further, we also note that quantum fluctuations around the “ordered state” due to \hat{H}_{Ω} may also lead to a change in its energy relative to the

QSL. It is this competition between kinetic energy and long-range interactions that we will study in this section.

We first show that the ground state in the classical limit $\Omega = 0$ is the zero-momentum state satisfying the ice rule which we call the “ice ferromagnet”. We assume that, as one increases Ω , there is no phase transition to a different ordered state before the putative transition to a QSL. In order to determine whether a QSL phase exists and, if yes, at what Ω the transition to the QSL occurs, one needs to compare the energies of ansatz wavefunctions of the QSL and the ordered state. When $\Omega \neq 0$, such wavefunctions would necessarily involve configurations that violate the ice rule. We incorporate the effect of nonzero Ω on the wavefunction using perturbation theory. Our strategy is as follows. We treat $\hat{H}_1 \equiv \hat{H}_\Omega + \hat{H}_{\text{LR}}$, i.e., both the laser driving term and the long-range interactions, as a perturbation to \hat{H}_0 (unlike Sec. II A, where we dropped \hat{H}_{LR}). We perturbatively find an effective Hamiltonian \hat{H}_{eff} acting on the low-energy ice manifold. We then compare the expectation value of \hat{H}_{eff} in candidate wavefunctions that live entirely in this low-energy space. Since a QSL wavefunction is a linear superposition of exponentially (in system size) many ice rule obeying states, we calculate $\langle \hat{H}_{\text{eff}} \rangle$ numerically using classical Monte Carlo sampling.

1. Expression for \hat{H}_{eff}

We perform a Schrieffer-Wolff transformation

$$\hat{H} = \hat{U}_S \hat{H} \hat{U}_S^\dagger = \hat{U}_S (\hat{H}_0 + \hat{H}_\Omega + \hat{H}_{\text{LR}}) \hat{U}_S^\dagger, \quad (19)$$

for a unitary $\hat{U}_S = e^{\hat{S}}$, where \hat{S} is an anti-hermitian operator chosen to make \hat{H} block-diagonal in the (degenerate) eigenbasis of \hat{H}_0 , i.e.,

$$\hat{H} = \hat{\mathcal{P}} \hat{H} \hat{\mathcal{P}} + (1 - \hat{\mathcal{P}}) \hat{H} (1 - \hat{\mathcal{P}}), \quad (20)$$

where $\hat{\mathcal{P}}$ projects onto the ice manifold. In the remainder of this paper, we will restrict ourselves to the low-energy sector and therefore only consider the $\hat{H}_{\text{eff}} \equiv \hat{\mathcal{P}} \hat{H} \hat{\mathcal{P}}$ term above. We calculate \hat{H}_{eff} perturbatively in $\hat{H}_1 = \hat{H}_\Omega + \hat{H}_{\text{LR}}$ (see Appendix B of Ref. [77] for general expressions of \hat{H}_{eff}). As we saw in Sec. II A, if we consider only \hat{H}_Ω as the perturbation, then the first non-trivial term appearing in \hat{H}_{eff} is $-J_{\text{ring}} \sum_{\text{O}} |\text{O}\rangle \langle \text{O}| + \text{H.c.}$, where

$$J_{\text{ring}} = \frac{63}{16} \frac{\Omega^6}{V^5} + \Theta\left(\frac{\Omega^8}{V^7}\right). \quad (21)$$

Since we are performing perturbation theory in two operators \hat{H}_Ω and \hat{H}_{LR} , each of them comes with its own small parameter. Since the perturbative expansion will involve polynomials in these two small parameters, there is some arbitrariness in deciding how to compare the two parameters relative to each other and thus in how to

truncate the expansion. In our calculation, we follow an operational scheme of keeping all the terms up to sixth order in $\hat{H}_\Omega + \hat{H}_{\text{LR}}$. Following this truncation scheme, we get (up to additive constants)

$$\begin{aligned} \hat{H}_{\text{eff}} \approx & -J_{\text{ring}} \sum_{\text{O}} |\text{O}\rangle \langle \text{O}| + \text{H.c.} \\ & + \left(1 - \frac{\Omega^2}{V^2} - \frac{61}{18} \frac{\Omega^4}{V^4}\right) \hat{H}_{\text{LR}} \\ & - \frac{\Omega^2}{V} \left(\hat{W}_{\text{LR}}^{(2)} + \hat{W}_{\text{LR}}^{(3)} + \hat{W}_{\text{LR}}^{(4)}\right) \\ & - \frac{\Omega^4}{V^3} \left(\frac{152}{27} \hat{W}_{\text{LR}}^{(2)} - \hat{L}_{\text{LR}}^{(2)} + \hat{M}_{\text{LR}}^{(2)}\right), \end{aligned} \quad (22)$$

where

$$\hat{W}_{\text{LR}}^{(2)} \equiv \frac{1}{4} \sum_j \sum_{\substack{k_1 \neq j \\ k_2 \neq j}} v_{j,k_1} v_{j,k_2} \hat{S}_{k_1}^z \hat{S}_{k_2}^z, \quad (23)$$

$$\hat{L}_{\text{LR}}^{(2)} \equiv \frac{109}{432} \sum_{\substack{j_1 \neq k_1 \\ j_2 \neq k_2}} \delta_{\langle j_1, j_2 \rangle} v_{j_1, k_1} v_{j_2, k_2} \hat{S}_{j_1}^z \hat{S}_{k_1}^z \hat{S}_{j_2}^z \hat{S}_{k_2}^z, \quad (24)$$

$$\hat{M}_{\text{LR}}^{(2)} \equiv \frac{20}{27} \sum_{\substack{j_1 \neq k_1 \\ j_2 \neq k_2}} \delta_{\langle j_1, j_2 \rangle} v_{j_1, k_1} v_{j_2, k_2} \hat{S}_{j_1}^z \hat{S}_{k_1}^z \hat{S}_{j_2}^z \hat{S}_{k_2}^z, \quad (25)$$

$$\hat{W}_{\text{LR}}^{(3)} \equiv \frac{1}{2} \sum_j \sum_{\substack{k_1 \neq j \\ k_2 \neq j \\ k_3 \neq j}} v_{j,k_1} v_{j,k_2} v_{j,k_3} \hat{S}_{k_1}^z \hat{S}_{k_2}^z \hat{S}_{k_3}^z \hat{S}_j^z, \quad (26)$$

$$\hat{W}_{\text{LR}}^{(4)} \equiv \frac{1}{4} \sum_j \sum_{\substack{k_1 \neq j \\ k_2 \neq j \\ k_3 \neq j \\ k_4 \neq j}} v_{j,k_1} v_{j,k_2} v_{j,k_3} v_{j,k_4} \hat{S}_{k_1}^z \hat{S}_{k_2}^z \hat{S}_{k_3}^z \hat{S}_{k_4}^z, \quad (27)$$

$$\text{and } v_{i,j} \equiv \begin{cases} \frac{a^6}{|\mathbf{x}_i - \mathbf{x}_j|^6} & \text{if } \mathbf{x}_i, \mathbf{x}_j \text{ are not nearest neighbors,} \\ 0 & \text{otherwise.} \end{cases} \quad (28)$$

In the above equations, $\delta_{\langle i,j \rangle}$ enforces i and j to be nearest neighbors.

The expectation value of the Hamiltonian (6) in a given state $|\Psi\rangle$ is

$$\langle \Psi | \hat{H} | \Psi \rangle = (\langle \Psi | \hat{U}_S^\dagger) (\hat{U}_S \hat{H} \hat{U}_S^\dagger) (\hat{U}_S | \Psi \rangle). \quad (29)$$

Suppose $\hat{U}_S |\Psi\rangle$ (i.e., $|\Psi\rangle$ transformed by the Schrieffer-Wolff transformation) lies entirely in the ice manifold, then using Eq. (19), we get

$$\langle \Psi | \hat{H} | \Psi \rangle = (\langle \Psi | \hat{U}_S^\dagger) \hat{H}_{\text{eff}} (\hat{U}_S | \Psi \rangle). \quad (30)$$

For the ground state, $|\Psi_g\rangle$ of the full Hamiltonian \hat{H} , $\hat{U}_S |\Psi_g\rangle$ lies entirely in the ice manifold. Thus, we pick an ansatz wavefunction for $\hat{U}_S |\Psi\rangle$ that also lies entirely in the ice manifold and compute the expectation value of \hat{H}_{eff} in our ansatz state to get the energy. Before describing our ansatz states in Sec. III A 3, we first consider the limit $\Omega = 0$ in the next section.

2. Classical ground state of the long-range Hamiltonian

Here, we will find the ground state selected by long-range interactions in the limit $\Omega = 0$ where there are no quantum fluctuations. The Hamiltonian is $\hat{H}_{\text{cl}} = \hat{H}_0 + \hat{H}_{LR}$. We find the ground state by going to the Fourier space. Since the pyrochlore lattice is an FCC lattice with a four-site basis, we use the notation $\hat{S}_{\mathbf{r},\mu}^z$ for spins where \mathbf{r} is an FCC lattice vector and $\mu \in \{0, 1, 2, 3\}$ labels the sites within the basis. The spin $\hat{S}_{\mathbf{r},\mu}^z$ is physically located at $\mathbf{r} + \mathbf{e}_\mu/2$ where \mathbf{e}_μ are the vectors joining a diamond A site to a neighboring diamond B site. (See Fig. 1(b) for the precise definition.) As we are considering the classical limit in this section, we drop hats on quantities which would otherwise be operators. The Fourier transform of $S_{\mathbf{r},\mu}^z$ is

$$S_{\mathbf{r},\mu}^z = \frac{1}{\sqrt{N_{\text{u.c.}}}} \sum_{\mathbf{k}} e^{i\mathbf{k}\cdot\mathbf{r}} S_{\mathbf{k},\mu}^z, \quad (31)$$

where $N_{\text{u.c.}}$ is the number of FCC unit cells. Substituting this in H_{cl} , we get

$$H_{\text{cl}} = \sum_{\mu,\nu,\mathbf{k}} V_{\mu\nu,\mathbf{k}} S_{\mathbf{k},\mu}^z S_{-\mathbf{k},\nu}^z, \quad (32)$$

where \mathbf{k} is a vector in the Brillouin zone of the FCC lattice and $V_{\mu\nu,\mathbf{k}}$ is the Fourier transform of the van der Waals potential:

$$V_{\mu\nu,\mathbf{k}} = \frac{V}{2} \sum_{\mathbf{r}} e^{i\mathbf{k}\cdot\mathbf{r}} \left(\frac{a}{|\mathbf{r} + (\mathbf{e}_\mu - \mathbf{e}_\nu)/2|} \right)^6. \quad (33)$$

Diagonalizing the matrix $V_{\mu\nu,\mathbf{k}}$ for each \mathbf{k} gives

$$H_{\text{cl}} = \sum_{\mu,\mathbf{k}} \varepsilon_{\mathbf{k},\mu} |S_{\mathbf{k},\mu}^z|^2, \quad (34)$$

where $S_{\mathbf{k},\mu}^z$ is related to $S_{\mathbf{k},\nu}^z$ through a multiplication by a unitary matrix $U_{\mu\nu,\mathbf{k}}$ which diagonalizes $V_{\mu\nu,\mathbf{k}}$: $S_{\mathbf{k},\mu}^z = \sum_{\nu} U_{\mu\nu,\mathbf{k}} S_{\mathbf{k},\nu}^z$. Recall that $S_{\mathbf{r},\mu}^z$ is either $+1/2$ or $-1/2$. This imposes the following constraint:

$$\sum_{\mathbf{k},\mu} |S_{\mathbf{k},\mu}^z|^2 = \sum_{\mathbf{k},\mu} |S_{\mathbf{k},\mu}^z|^2 = \sum_{\mathbf{r},\mu} (S_{\mathbf{r},\mu}^z)^2 = N_{\text{u.c.}}. \quad (35)$$

From Eq. (34), the energy can be interpreted as a weighted sum of $\varepsilon_{\mathbf{k},\mu}$ with the corresponding weights being $|S_{\mathbf{k},\mu}^z|^2$. Because of the constraint in Eq. (35), the energy is minimized by having the full weight on the smallest $\varepsilon_{\mathbf{k},\mu}$ and no weight on the rest of the $\varepsilon_{\mathbf{k},\mu}$. This holds provided that such a configuration of $S_{\mathbf{k},\mu}^z$ in the momentum space corresponds to some configuration in the real space where $S_{\mathbf{r},\mu}^z$ are $\pm 1/2$.

Calculating the Fourier transform of the long-range potential, Eq. (33), and its eigenvalues $\varepsilon_{\mathbf{k},\mu}$, we find that the

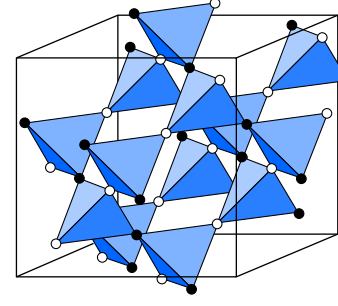


Figure 7: An ice ferromagnet state. It is an ice rule obeying state (i.e., $n_{\Delta} = 2$ on every tetrahedron) with $\mathbf{k} = \mathbf{0}$. All the up-pointing tetrahedra are copies of each other. The same is true for the down-pointing tetrahedra. There are six (4C_2) such states, and together they make up the ground subspace of \hat{H}_{cl} .

minimum of $\varepsilon_{\mathbf{k},\mu}$ occurs for $\mathbf{k} = \mathbf{0}$ and is triply degenerate. In particular,

$$V_{\mu\nu,\mathbf{k}=\mathbf{0}} = \begin{pmatrix} v_1 & v_2 & v_2 & v_2 \\ v_2 & v_1 & v_2 & v_2 \\ v_2 & v_2 & v_1 & v_2 \\ v_2 & v_2 & v_2 & v_1 \end{pmatrix}, \quad (36)$$

where $v_1 = 0.113V$ and $v_2 = 1.12V$. Its eigenvalues are $\varepsilon_{\mathbf{0},0} = 3.46V$ and $\varepsilon_{\mathbf{0},1} = \varepsilon_{\mathbf{0},2} = \varepsilon_{\mathbf{0},3} = -1.004V$. The unitary that diagonalizes the above matrix also relates $S_{\mathbf{0},\mu}^z$ to $S_{\mathbf{0},\nu}^z$ as

$$\begin{pmatrix} S_{\mathbf{0},0}^z \\ S_{\mathbf{0},1}^z \\ S_{\mathbf{0},2}^z \\ S_{\mathbf{0},3}^z \end{pmatrix} = \frac{1}{2} \begin{pmatrix} 1 & 1 & 1 & 1 \\ 1 & 1 & -1 & -1 \\ 1 & -1 & 1 & -1 \\ 1 & -1 & -1 & 1 \end{pmatrix} \begin{pmatrix} S_{\mathbf{0},0}^z \\ S_{\mathbf{0},1}^z \\ S_{\mathbf{0},2}^z \\ S_{\mathbf{0},3}^z \end{pmatrix}. \quad (37)$$

Since $\varepsilon_{\mathbf{0},1}$, $\varepsilon_{\mathbf{0},2}$ and $\varepsilon_{\mathbf{0},3}$ are the minimum eigenvalues, the energy is minimized by having all the weight distributed between $S_{\mathbf{0},1}^z$, $S_{\mathbf{0},2}^z$ and $S_{\mathbf{0},3}^z$ and no weight on the remaining $S_{\mathbf{k},\mu}^z$, that is, $S_{\mathbf{k}\neq\mathbf{0},\mu}^z = 0$ and $S_{\mathbf{0},0}^z = 0$. There indeed exist states satisfying these two conditions. The first condition, $S_{\mathbf{k}\neq\mathbf{0},\mu}^z = 0$, implies that the ground state is a $\mathbf{k} = \mathbf{0}$ state, while the second condition, $S_{\mathbf{0},0}^z = 0$, implies that the ground state satisfies the ice rule (so that the total spin, which is $S_{\mathbf{0},0}^z$ is 0), see Eq. (37). There are six such states, and we refer to them as the “ice ferromagnet” or “ice FM” states. One of these is shown in Fig. 7.

3. Ansatz wavefunctions for the ordered state and for the quantum spin liquid

We now assume that, as one increases Ω starting from $\Omega = 0$, the ground state remains adiabatically connected to the ice ferromagnet derived in the previous section till

the point where it undergoes the putative phase transition to the QSL. Therefore, our ansatz for the ordered state is

$$|\Psi_{\text{ord}}\rangle = \hat{U}_S^\dagger |\Psi_{\text{IFM}}\rangle, \quad (38)$$

where $|\Psi_{\text{IFM}}\rangle$, a product state in the \hat{S}^z basis, is the $\mathbf{k} = \mathbf{0}$ ice ferromagnet defined Sec. III A 2. This configuration is given by $S_{\mathbf{r},\mu}^z = \frac{1}{2}\varepsilon_\mu$ (independent of \mathbf{r}), where $(\varepsilon_0, \varepsilon_1, \varepsilon_2, \varepsilon_3) \equiv (1, 1, -1, -1)$. We note that there are six such choices for ε_μ that satisfy the ice rule. We pick one such choice, but our calculations are not sensitive to which one we pick. $|\Psi_{\text{IFM}}\rangle$ lives entirely in the ice manifold. Left-multiplication by \hat{U}_S^\dagger takes it back to the original Hilbert space with ice rule violations.

Our ansatz wave function for the spin liquid state is

$$|\Psi_{\text{QSL}}\rangle = \hat{U}_S^\dagger |\Psi_{\text{RK}}\rangle, \quad (39)$$

where $|\Psi_{\text{RK}}\rangle$ is a uniform superposition of all dimer coverings [65] of the diamond lattice (with $n_\Delta = 2$). $|\Psi_{\text{RK}}\rangle$ lives in the ice manifold. Like before, we left-multiply it by \hat{U}_S^\dagger to take it back to the original Hilbert space. The justification for our choice is the following. $|\Psi_{\text{RK}}\rangle$ is the ground state of the dimer model at the RK point [see Eq. (10)]. When the RK potential is zero, $|\Psi_{\text{RK}}\rangle$ has an energy expectation value of $-4N_{\text{u.c.}}J_{\text{ring}}\bar{n}_{\text{flip}}$, where \bar{n}_{flip} is the average fraction of flippable hexagons in the RK wavefunction. We find numerically that $\bar{n}_{\text{flip}} = 0.1757$ (also calculated in Ref. [48]). Therefore, the energy of $|\Psi_{\text{RK}}\rangle$ is $-0.7028J_{\text{ring}}N_{\text{u.c.}}$ which is not too far from the ground state energy of the dimer model (12) found in Ref. [51] to be $-0.756J_{\text{ring}}N_{\text{u.c.}}$. Even though $|\Psi_{\text{RK}}\rangle$ has slightly higher energy, it has the advantage of being simpler to sample by classical Monte Carlo. This explains our choice.

For comparison, we will also calculate the energy of a different ordered state $|\Psi_{\text{ord}}\rangle = \hat{U}_S^\dagger |\Psi_{\text{IAFM}}\rangle$ that we call an ice antiferromagnet. Here $|\Psi_{\text{IAFM}}\rangle$ is an ice rule obeying state with ordering wave vector $\mathbf{k} = \pi(\mathbf{b}_1 + \mathbf{b}_2)$, where $\mathbf{b}_1, \mathbf{b}_2$ and \mathbf{b}_3 are primitive reciprocal lattice vectors of the FCC lattice satisfying $\mathbf{a}_i \cdot \mathbf{b}_j = \delta_{ij}$. This state is known elsewhere in literature as the $2\pi(001)$ state (this nomenclature uses an enlarged cubic unit cell of the FCC lattice) [76, 78, 79].

4. Numerical results—energy expectation values and phase diagram

We now describe our computation of the expectation value of \hat{H}_{eff} [see Eq. (22)] in $|\Psi_{\text{RK}}\rangle$, $|\Psi_{\text{IFM}}\rangle$ and in $|\Psi_{\text{IAFM}}\rangle$. While the expectation value in $|\Psi_{\text{IFM}}\rangle$ and $|\Psi_{\text{IAFM}}\rangle$ can be computed straightforwardly, the expectation value in $|\Psi_{\text{RK}}\rangle$ requires classical Monte Carlo sampling. We use a system with $8 \times 8 \times 8$ unit cells (i.e., containing 2048 pyrochlore sites) with periodic boundary conditions in the $\mathbf{a}_1, \mathbf{a}_2$, and \mathbf{a}_3 directions. We restrict our sampling to sectors in which the total electric flux

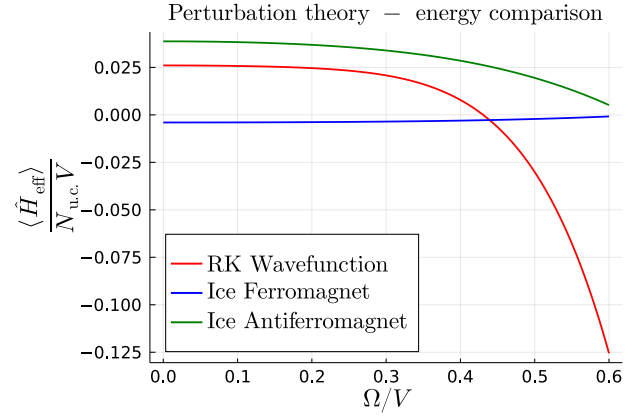


Figure 8: $\langle \hat{H}_{\text{eff}} \rangle$ in $|\Psi_{\text{RK}}\rangle$, $|\Psi_{\text{IFM}}\rangle$, and $|\Psi_{\text{IAFM}}\rangle$ calculated by inserting the values in Table I in Eq. (22).

piercing through any 2D torus cross-section (as defined in Sec. IV B of Ref. [48]) is 0. Our sampling is done using loop moves as described in Refs. [48, 78, 79]—in each Monte Carlo run, we perform $512 \times 500,000$ loop moves. We calculate \bar{n}_{flip} , H_{LR} , $W_{\text{LR}}^{(2)}$ and $L_{\text{LR}}^{(2)}$ after every 512 loop moves, i.e., we take 500,000 data points. We calculate $M_{\text{LR}}^{(2)}$, $W_{\text{LR}}^{(3)}$, and $W_{\text{LR}}^{(4)}$ after every $512 \times 10,000$ loop moves, i.e. we take 50 data points. We repeat this procedure for 9 independent runs in order to calculate the uncertainties. Our results are summarized in Table I. With these values at hand, we calculate the expectation value of \hat{H}_{eff} using Eq. (22) in $|\Psi_{\text{RK}}\rangle$, $|\Psi_{\text{IFM}}\rangle$, and $|\Psi_{\text{IAFM}}\rangle$, and the result is plotted in Fig. 8. As we turn on Ω , the transition point Ω_C can be determined within our approximation as the Ω for which the energy of the ice ferromagnet becomes higher than that of the RK wavefunction, as calculated using Eq. (22). We find

$$\Omega_C = 0.43927(1)V. \quad (40)$$

There is an important question on whether our use of perturbation theory is justified. First, we argue that treating \hat{H}_{LR} perturbatively is justified. $\{\hat{H}_{\text{LR}}\}$, $\{\hat{W}_{\text{LR}}^{(2)}, \hat{L}_{\text{LR}}^{(2)}, \hat{M}_{\text{LR}}^{(2)}\}$, $\{\hat{W}_{\text{LR}}^{(3)}\}$, and $\{\hat{W}_{\text{LR}}^{(4)}\}$ are sets of operators that are first, second, third, and fourth order respectively in \hat{H}_{LR} . As we can see from Table I, the expectation values of these operators in $|\Psi\rangle_{\text{RK}}$ drops by an order of magnitude each time one goes one order higher in \hat{H}_{LR} . Next, is perturbation theory in \hat{H}_Ω justified, given that our calculated Ω_C is outside the $\Omega \ll V$ regime? We observe that the leading contribution to J_{ring} that we dropped, $\frac{33833}{2592} \frac{(\Omega_C)^8}{V^7} = 0.018V$ [74], is smaller than the one we kept, $\frac{63}{16} \frac{(\Omega_C)^6}{V^5} = 0.028V$. If we had kept higher order contributions to J_{ring} , it would only decrease the energy of the QSL relative to the ice ferromagnet and ice antiferromagnet. Further, the energy of the QSL that we present is a conservative estimate since we used the RK wavefunction which has higher energy than the true ground state of Hamiltonian (9). This gives us hope that

Operator	$ \Psi_{\text{RK}}\rangle$	$ \Psi_{\text{IFM}}\rangle$	$ \Psi_{\text{IAFM}}\rangle$
\hat{R}	$0.70288(4)N_{\text{u.c.}}$	0	0
\hat{H}_{LR}	$2.6037(1) \times 10^{-2}N_{\text{u.c.}}$	$-0.4002 \times 10^{-2}N_{\text{u.c.}}$	$3.8722 \times 10^{-2}N_{\text{u.c.}}$
$\hat{W}_{\text{LR}}^{(2)}$	$1.11778(1) \times 10^{-3}N_{\text{u.c.}}$	$0.01642 \times 10^{-3}N_{\text{u.c.}}$	$1.4994 \times 10^{-3}N_{\text{u.c.}}$
$\hat{L}_{\text{LR}}^{(2)}$	$-2.7467(3) \times 10^{-4}N_{\text{u.c.}}$	$-0.0829 \times 10^{-4}N_{\text{u.c.}}$	$-7.5662 \times 10^{-4}N_{\text{u.c.}}$
$\hat{M}_{\text{LR}}^{(2)}$	$2.96(3) \times 10^{-3}N_{\text{u.c.}}$	$0.073 \times 10^{-3}N_{\text{u.c.}}$	$6.66 \times 10^{-3}N_{\text{u.c.}}$
$\hat{W}_{\text{LR}}^{(3)}$	$5.25(4) \times 10^{-5}N_{\text{u.c.}}$	$-0.00665 \times 10^{-5}N_{\text{u.c.}}$	$5.81 \times 10^{-5}N_{\text{u.c.}}$
$\hat{W}_{\text{LR}}^{(4)}$	$-3.57(2) \times 10^{-6}N_{\text{u.c.}}$	$-0.0309 \times 10^{-6}N_{\text{u.c.}}$	$-5.35 \times 10^{-6}N_{\text{u.c.}}$

Table I: The expectation values of the operators in the left column in ansatz wavefunctions $|\Psi_{\text{RK}}\rangle$, $|\Psi_{\text{IFM}}\rangle$ and $|\Psi_{\text{IAFM}}\rangle$ respectively. The operator \hat{R} is defined as $\hat{R} = \sum_{\square} |\square\rangle \langle \square| + \text{H.c.}$ In the RK wavefunction, $\langle \Psi_{\text{RK}} | \hat{R} | \Psi_{\text{RK}} \rangle = 4\bar{n}_{\text{flip}} N_{\text{u.c.}}$. To calculate expectation values in $|\Psi_{\text{RK}}\rangle$, we have used classical Monte Carlo sampling.

our result obtained using perturbation theory is qualitatively correct.

Within our approximation, for $\Omega < \Omega_C$, the ground state is an ice ferromagnet, an ordered state satisfying the ice rule. For $\Omega > \Omega_C$ but also close to Ω_C , the ground state is in the QSL phase, i.e., the deconfined phase of a $U(1)$ gauge theory. From the point of view of the QSL, the ordered ice ferromagnet state is obtained when monopole excitations of the spin liquid proliferate, and the monopole-antimonopole string operator, to be defined in Sec. IV B, Eq. (53), acquires an expectation value. As a consequence of this, the fractional “electric charges”, or spinons, get confined [46, 47]. The monopole creation operator (see Sec. IV B and Ref. [48]) is diagonal in the \hat{S}^z basis, and acts in the sector that obeys the ice rule. It is thus plausible that the confined phase is indeed the ice ferromagnet. While our calculation provides microscopic intuition for this transition, we emphasize that, to prove the existence of, locate and characterize this transition accurately, one needs to do a more careful quantum Monte Carlo calculation.

B. Large Ω —Higgs transition

From the Hamiltonian in Eq. (6), it is clear that, in the limit $\Omega \gg V$, the ground state is a transverse-field-polarized (TFP) state, i.e., a product state of $(|g\rangle - |r\rangle)_i$ at each site i . Thus, as Ω is increased away from Ω_C , the system should eventually go through a phase transition from the putative QSL phase into the TFP phase. From the point of view of the QSL, this is a Higgs transition because the operator \hat{S}^x that acquires expectation value in the TFP phase creates a pair of “electric”-charge excitations in the spin liquid. The perturbation theory in Ω/V that we performed in Sec. III A relies on the ability to go to a basis where the Hilbert space decouples into ice rule obeying and ice rule disobeying sectors separated by an energy gap of V . But the ground state in the $\Omega \gg V$ limit (TFP) straddles both of these sectors. So we do not expect perturbation theory in Ω/V to capture the phase

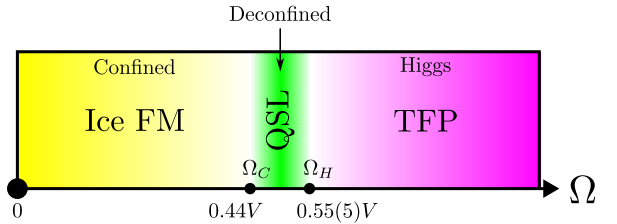


Figure 9: Approximate ground state phase diagram of the Hamiltonian in Eq. (6). The ground state for $\Omega = 0$ was calculated exactly to be an ice ferromagnet (ice FM) in Sec. III A 2. We assume that, as Ω is increased, no phase transition occurs to a different ordered state. The transition point from the ice ferromagnet (confined phase) to the QSL (deconfined phase) at $\Omega_C \approx 0.44V$ is obtained by comparing energies of ansatz wavefunctions in the effective Hamiltonian obtained using perturbation theory in \hat{H}_Ω and \hat{H}_{LR} . For the Higgs transition to the TFP phase, we make an approximation by dropping \hat{H}_{LR} , in which case Ω_H was calculated in Ref. [62] to be $0.55(5)$.

transition into the TFP phase that contains the $\Omega \rightarrow \infty$ ground state. Hence, we will present an indirect reasoning below. In the $\Omega \ll V$ limit, \hat{H}_{LR} was important, since it was the dominant term splitting the degeneracy in the ice manifold. On the other hand, in the vicinity of the putative Higgs transition, \hat{H}_{LR} may not be as important since the largest term in \hat{H}_{LR} has magnitude $V/27$, and as justified above using Table I, the effect of \hat{H}_{LR} is indeed perturbative. Therefore, we drop \hat{H}_{LR} as a zeroth-order approximation for calculating the Higgs transition point. The resulting Hamiltonian is the transverse field Ising model on the pyrochlore lattice. Refs. [62] and [74] studied this model and found the transition point Ω_H to be at $\Omega_H = 0.55(5)V$ and $0.6V$ respectively. This leads us to expect that, in the window $0.44 < \Omega < 0.55$, the ground state may be a QSL, leading us to sketch the phase diagram shown in Fig. 9. Within our approximation, $\Omega_C < \Omega_H$ and there is a window where the QSL

is the ground state. However, the introduction of \hat{H}_{LR} may result in a lowering of the energy of the TFP state relative to the QSL. Calculating this effect and verifying that this does not bring down Ω_H far enough to destroy the QSL phase requires a more careful calculation which is beyond the scope of this work.

In the remainder of this section, we provide some intuition for the Higgs transition by performing a gauge mean field theory (gMFT) calculation introduced in Ref. [80].

1. Gauge mean field theory—Higgs transition

The main idea of this approach is to first recast the microscopic Hamiltonian as an exact gauge theory by introducing ancillary degrees of freedom followed by a mean-field decoupling of the interactions. This theory involves bosonic charges hopping in the presence of a fluctuating gauge field whose mean-field value is chosen self-consistently. If this mean-field gauge-field configuration is such that the hopping amplitudes of the bosonic charges is 0, then the theory is in a confined phase. If not, the theory is in the deconfined phase as long as the bosons do not condense. If the bosonic charges condense, then the theory is in a Higgs phase, which is adiabatically connected to the TFP state.

Concretely, the construction is as follows. For $\mathbf{r} \in A$, where A is a sublattice of the diamond lattice,

$$\hat{S}_{\mathbf{r} \rightarrow \mathbf{r} + \mathbf{e}_\mu}^+ = \hat{\Phi}_{\mathbf{r}}^\dagger \hat{s}_{\mathbf{r} \rightarrow \mathbf{r} + \mathbf{e}_\mu}^+ \hat{\Phi}_{\mathbf{r} + \mathbf{e}_\mu}, \quad (41)$$

where $\hat{S}_{\mathbf{r} \rightarrow \mathbf{r} + \mathbf{e}_\mu}^+ \equiv \hat{S}_{\mathbf{r} + \mathbf{e}_\mu/2}^+ = \hat{s}_{\mathbf{r},\mu}^+$ (and similarly $\hat{s}_{\mathbf{r} \rightarrow \mathbf{r} + \mathbf{e}_\mu}^+ \equiv \hat{s}_{\mathbf{r} + \mathbf{e}_\mu/2}^+ = \hat{s}_{\mathbf{r},\mu}^+$) lives on a bond of the diamond lattice connecting sites \mathbf{r} and $\mathbf{r} + \mathbf{e}_\mu$ (recall that centers of the bonds of the diamond lattice are sites of the pyrochlore lattice). \hat{s}^z is also a spin-1/2 operator and has eigenvalues $\pm 1/2$. Here, $\hat{\Phi}_{\mathbf{r}}^\dagger$ serves as a raising operator for $\hat{Q}_{\mathbf{r}} \equiv \eta_{\mathbf{r}}(\hat{n}_{\mathbf{r}} - 2)$, where $\eta_{\mathbf{r}} = 1$ for $\mathbf{r} \in A$ and $\eta_{\mathbf{r}} = -1$ for $\mathbf{r} \in B$. For convenience, we drop the symbol $\hat{\Delta}$ from now on. $\hat{Q}_{\mathbf{r}}$ and $\hat{\Phi}_{\mathbf{r}}^\dagger$ satisfy the commutation relation: $[\hat{Q}_{\mathbf{r}}, \hat{\Phi}_{\mathbf{r}}^\dagger] = \hat{\Phi}_{\mathbf{r}}^\dagger$. Note that $\hat{\Phi}_{\mathbf{r}}$ is not a canonical boson but a rotor satisfying

$$\hat{\Phi}_{\mathbf{r}}^\dagger \hat{\Phi}_{\mathbf{r}} = 1. \quad (42)$$

To recover the original spin Hilbert space, one imposes the constraint that the total gauge charge at \mathbf{r} is

$$\hat{Q}_{\mathbf{r}} = \eta_{\mathbf{r}} \sum_{\mu} \hat{s}_{\mathbf{r} + \eta \mathbf{e}_\mu/2}^z. \quad (43)$$

Rewriting the Hamiltonian (6) in terms of the fictitious variables, $\hat{Q}_{\mathbf{r}}$, $\hat{\Phi}_{\mathbf{r}}$ and $\hat{s}_{\mathbf{r},\mu}$ we get

$$\begin{aligned} \hat{H} = & \frac{V}{2} \sum_{\mathbf{r} \in A, B} \hat{Q}_{\mathbf{r}}^2 - \frac{\Omega}{2} \sum_{(\mathbf{r} \in A), \mu} \left(\hat{\Phi}_{\mathbf{r}}^\dagger \hat{s}_{\mathbf{r} \rightarrow \mathbf{r} + \mathbf{e}_\mu}^+ \hat{\Phi}_{\mathbf{r} + \mathbf{e}_\mu} + \text{H.c.} \right) \\ & + \frac{1}{2} \sum_{\mathbf{r}, \mathbf{r}' \in A} \sum_{\mu, \nu} V_{\mu\nu}(\mathbf{r} - \mathbf{r}') \hat{s}_{\mathbf{r}\mu}^z \hat{s}_{\mathbf{r}',\nu}^z, \end{aligned} \quad (44)$$

where $V_{\mu\nu}(\mathbf{r} - \mathbf{r}') = V \left(\frac{a}{\mathbf{r} - \mathbf{r}' + \mathbf{e}_\mu/2 - \mathbf{e}_\nu/2} \right)^6$ whenever (\mathbf{r}, μ) and (\mathbf{r}', ν) are distinct and are not nearest-neighbors. $V_{\mu\nu}(\mathbf{r} - \mathbf{r}')$ is 0 otherwise.

Following Ref. [80], we perform the zeroth-order mean-field decoupling: $\hat{\Phi}^\dagger \hat{\Phi} \hat{s} \rightarrow \hat{\Phi}^\dagger \hat{\Phi} \langle \hat{s} \rangle + \langle \hat{\Phi}^\dagger \hat{\Phi} \rangle \hat{s} - \langle \hat{\Phi}^\dagger \hat{\Phi} \rangle \langle \hat{s} \rangle$ and $\hat{s} \hat{s} \rightarrow \hat{s} \langle \hat{s} \rangle + \langle \hat{s} \rangle \hat{s} - \langle \hat{s} \rangle \langle \hat{s} \rangle$ (where \hat{s} could either be \hat{s}^+ , \hat{s}^- , or \hat{s}^z). Upon doing so, the Hamiltonian decouples into a Hamiltonian of bosons hopping on the diamond lattice and a Hamiltonian of spins in an external field, which itself is set self-consistently by the Green's function of the bosons. Before solving the resulting theory, one needs to enforce the constraints (42) and (43) using Lagrange multipliers $\lambda_{\mathbf{r}}$ and $v_{\mathbf{r}}$, respectively. Within the mean-field theory, it is assumed that these Lagrange multipliers take a spatially homogeneous value at the saddle point. We then find the minimum value of Ω_H^{MF} such that, for any $\Omega > \Omega_H^{\text{MF}}$, it is possible to self-consistently choose λ only by macroscopically occupying a boson mode. This Ω_H^{MF} marks the location of the Bose-Einstein-condensation transition (or Higgs transition within the mean-field theory). We find $\Omega_H^{\text{MF}} \approx 0.7V$. In Appendix A, we present more details of this calculation. An artifact of this technique is that, although we include long-range interactions in our calculation, they do not play any role at the saddle point near the Higgs transition. Therefore, the final steps and result of our calculation are identical to the ones carried out in [68].

In Appendix A, we also point out a major limitation of this technique in the small- Ω limit that may not have been appreciated in previous literature on gauge mean field theory.

C. Comments on dynamical state preparation

So far, we have focused on the nature of the ground state of Hamiltonian (6) as a function of Ω/V . However, what is often experimentally relevant is the nature of the state prepared by a ramping of parameters in a finite amount of time. This issue was studied in Ref. [81] for a \mathbb{Z}_2 gauge theory in the context of the experiment in Ref. [26]. Since the main ideas of Ref. [81] are general enough, here we will present an adaptation of the conclusions of Ref. [81] to our setting.

The excitations of a $U(1)$ QSL are gapless “photons”, magnetic monopoles, and “electric charges” (spinons). The transition of a QSL to an ice ferromagnet is driven by the condensation of monopoles, while the transition to the TFP phase is driven by the condensation of spinons. The gapless “photons” are not directly involved in these transitions. Also, a state with “photon” modes excited on top of a QSL state is still in the deconfined phase of the $U(1)$ gauge theory. This allows us to ignore “photons” in this section. Since the confined phase, ice ferromagnet has an extensive number of monopoles, we use the difference per unit cell between the energies of

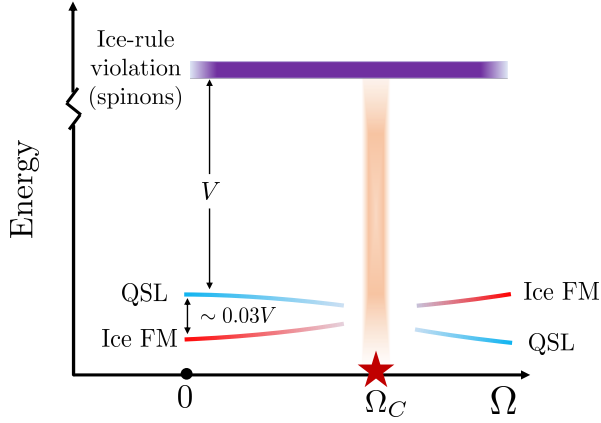


Figure 10: A qualitative sketch of the energy scales (per unit cell) in our problem. For $\Omega > \Omega_C$, the ground state is a $U(1)$ QSL. Ice ferromagnet is the ordered state obtained when monopoles proliferate, i.e., the ice ferromagnet has an extensive number of monopoles. We therefore use the energy difference per unit cell between the QSL and the ice ferromagnet at $\Omega = 0$, obtained in Table I, as a proxy for the monopole energy scale. This scale $\sim 0.03V$ is much smaller than the spinon energy scale (“electric charge”), which is $\sim V$.

the QSL and ice ferromagnet states as a proxy for the monopole energy scale. At $\Omega = 0$, this difference is $(\langle \hat{H}_{LR} \rangle_{QSL} - \langle \hat{H}_{LR} \rangle_{IFM}) / N_{u.c.} \approx 0.03V$ (see Table I), which is much smaller than the spinon energy scale (see Fig. 10 for a sketch). Suppose one starts with an initial state (for a small $\epsilon \sim \Omega/V$)

$$|\Psi_{(t=0)}\rangle = \otimes_i (|g\rangle_i + \epsilon |r\rangle_i), \quad (45)$$

which is the ground state in the limit of large negative δ/V and small Ω/V . As shown in Sec. II, the classical ground state lies in the ice manifold when $\delta \in (2.46V, 4.46V)$. Now suppose that δ is ramped up from its initial large negative value to a value in this range such that the ramp is adiabatic with respect to the spinon gap V , but is sudden with respect to the monopole scale $\sim 0.03V$, while keeping $\Omega/V \ll 1$. Using arguments in Ref. [81], this protocol will not prepare the ground state, which, from Fig. 9, is an ice ferromagnet. Instead, it will (approximately) project out violations of the ice rule (due to adiabaticity with respect to the spinon scale) from the initial state $|\Psi_{(t=0)}\rangle$. The resulting final state is

$$|\Psi_{\text{final}}\rangle \approx \hat{\mathcal{P}} \{ \otimes_i (|g\rangle_i + \epsilon |r\rangle_i) \} = |\Psi_{\text{RK}}\rangle, \quad (46)$$

where $\hat{\mathcal{P}}$ is the projector onto the ice manifold. The projected wavefunction is an equal-weight superposition of all coverings, which is simply the RK wavefunction and which lies in the QSL phase [48]. There is one catch to the above argument—the spinon gap closes during the above ramp. So it is impossible to be sudden with respect to the monopole scale and yet be strictly adiabatic with respect

to the spinon gap throughout the ramp. For a short duration (while the ramp is going through the spinon gap closing), adiabaticity with respect to the spinon gap will be violated. By the Kibble-Zurek mechanism, the resulting state is composed of finite-size puddles of QSL-like regions with a nonzero density of spinons interspersed [81–84]. Thus, in summary, there are two different ways in which one can prepare a $U(1)$ QSL-like state in experiment and study a confinement-deconfinement transition¹.

1. $\Omega/V \ll 1$: Perform a ramp of δ starting from a large negative value and ending in the range $(2.46V, 4.46V)$ for a fixed $\Omega/V \ll 1$ such that the ramp is adiabatic with respect to V (spinon gap) but sudden with respect to the monopole scale ($\sim 0.03V$). Even though the ground state is not a QSL for these parameters, this procedure would create puddles of QSL-like regions by the argument in Ref. [81]. To see a deconfinement-confinement transition, the ramp of δ should be slowed down and, once it is adiabatic with respect to the monopole gap, an ordered, i.e. confined state will be prepared.
2. Adiabatic: Perform a ramp of δ starting from a large negative value and ending in the range $(2.46V, 4.46V)$ and a ramp in Ω starting from $\Omega/V \ll 1$ and ending in a final value Ω_f , such that both ramps are adiabatic with respect to the monopole scale always. The two ramps can be performed simultaneously, or such that the ramp in δ precedes the ramp in Ω . This would approximately create the ground state of Hamiltonian (6). As the final value Ω_f goes through Ω_C (Ω_H), the nature of the final state prepared this way goes through a confinement-deconfinement (Higgs) transition.

Once a state is prepared by either of the above schemes, one needs to devise measurements that can tell whether the state is in the confined phase or in the deconfined phase. We address this in the following section.

IV. DIAGNOSIS OF THE QUANTUM SPIN LIQUID

Access to wavefunction snapshots in the \hat{S}^z basis, combined with access to unitary evolution, allows one to use the Rydberg-atom platform to measure non-local observables, a feature generally unavailable in traditional condensed matter systems. In this section, we describe some

¹ We note that the confinement-deconfinement transition of $U(1)$ gauge theory in 3+1D is strictly speaking, a ground state transition [71, 85]. Therefore, in this paper, when we use the phrase confinement-deconfinement transition, we mean signatures of this transition in a finite-size state prepared in finite time.

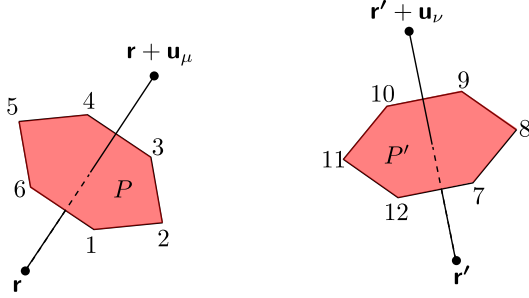


Figure 11: Notation for the plaquette correlators. P and P' are two hexagonal plaquettes of the pyrochlore lattice. \mathbf{r} , \mathbf{r}' , $\mathbf{r} + \mathbf{u}_\mu$, and $\mathbf{r}' + \mathbf{u}_\nu$ are the sites of the dual diamond lattice. \mathbf{u}_μ and \mathbf{u}_ν are vectors perpendicular to P and P' .

measurable correlators which can be used to observe the signatures of a quantum spin liquid state. In this section, we assume that the detuning is chosen such that $\rho = 2$.

A. Plaquette-plaquette correlators

The plaquette operators are off-diagonal in the \hat{S}^z basis and map one dimer covering to another. They are important in distinguishing a coherent quantum superposition from a classical admixture of states. We define two plaquette operators \hat{X}_P and \hat{Y}_P for a hexagonal plaquette P of the pyrochlore lattice as

$$\begin{aligned}\hat{X}_P &= (\hat{S}_1^+ \hat{S}_2^- \hat{S}_3^+ \hat{S}_4^- \hat{S}_5^+ \hat{S}_6^- + \text{H.c.}), \\ \hat{Y}_P &= -i \hat{S}_1^+ \hat{S}_2^- \hat{S}_3^+ \hat{S}_4^- \hat{S}_5^+ \hat{S}_6^- + \text{H.c.},\end{aligned}\quad (47)$$

where $1, 2, \dots, 6$ denote the sites around a plaquette P . Either of the two correlators, $\langle \hat{X}_P \hat{X}_{P'} \rangle$ and $\langle \hat{Y}_P \hat{Y}_{P'} \rangle$, of the plaquette operators on two plaquettes P and P' can distinguish a QSL phase from other phases including a classical spin ice (see Table II). We compare the two correlators and provide protocols to measure them. We assume throughout that the two plaquettes P and P' do not have any sites in common.

Using the mapping between the spins and the effective $U(1)$ gauge theory from Eq. (13), we see that the operators \hat{X}_P and \hat{Y}_P are equal to (twice) the cosine and the sine of the magnetic field, respectively:

$$\begin{aligned}\hat{X}_P &= 2 \cos(\hat{\theta}_1 - \hat{\theta}_2 + \hat{\theta}_3 - \hat{\theta}_4 + \hat{\theta}_5 - \hat{\theta}_6) = 2 \cos(\hat{b}_{\mathbf{r},\mu}), \\ \hat{Y}_P &= 2 \sin(\hat{\theta}_1 - \hat{\theta}_2 + \hat{\theta}_3 - \hat{\theta}_4 + \hat{\theta}_5 - \hat{\theta}_6) = 2 \sin(\hat{b}_{\mathbf{r},\mu}),\end{aligned}\quad (48)$$

where \mathbf{r} belongs to the dual diamond lattice [see Fig. 1(c)], and $\mu \in \{0, 1, 2, 3\}$ labels the direction of magnetic field. $\hat{b}_{\mathbf{r},\mu}$ is along \mathbf{u}_μ , which are vectors joining an A site of the dual diamond lattice to its neighboring B sites. These vectors are perpendicular to the plaquettes of the pyrochlore lattice, see Fig. 11. The effective theory in the deconfined phase (QSL) is Maxwell electromagnetism.

In the $3 + 1$ D continuum Maxwell electromagnetism, the correlators of the Cartesian components of the magnetic field $\hat{b}_{\mathbf{r},i}$ for $i \in \{x, y, z\}$ can be expressed as Gaussian integrals which evaluate to [48]

$$\langle \hat{b}_{\mathbf{0},i} \hat{b}_{\mathbf{R},j} \rangle_0 \propto \frac{1}{\mathbf{R}^4} \left(2 \frac{\mathbf{R}_i \mathbf{R}_j}{\mathbf{R}^2} - \delta_{ij} \right) \equiv \mathcal{C}_{ij}^B(\mathbf{R}), \quad (49)$$

where $\langle \cdot \rangle_0$ is the expectation value with respect to the Maxwell action.

The correlators of the magnetic field operators $\hat{b}_{\mathbf{r},\mu}$ for $\mu \in \{0, 1, 2, 3\}$ on the pyrochlore plaquettes in the deconfined phase are obtained from Eq. (49) by taking components of the Cartesian magnetic field along the vectors \mathbf{u}_μ . The result is

$$\begin{aligned}\langle \hat{X}_P \hat{X}_{P'} \rangle - 4 &\propto \frac{1}{\mathbf{R}^8} \left[\sum_{k,l} (\mathbf{u}_\mu)_k (\mathbf{u}_\nu)_l \left(2 \frac{\mathbf{R}_l \mathbf{R}_k}{\mathbf{R}^2} - \delta_{k,l} \right) \right], \\ \langle \hat{Y}_P \hat{Y}_{P'} \rangle &\propto \frac{1}{\mathbf{R}^4} \left[\sum_{k,l} (\mathbf{u}_\mu)_k (\mathbf{u}_\nu)_l \left(2 \frac{\mathbf{R}_l \mathbf{R}_k}{\mathbf{R}^2} - \delta_{k,l} \right) \right],\end{aligned}\quad (50)$$

where the summation is over $k, l \in \{x, y, z\}$, $\mathbf{R} = \mathbf{r} - \mathbf{r}'$, and \mathbf{R} is assumed to be large compared to the monopole correlation length. The factors inside the square brackets are geometric factors, which depend on the direction of the vectors \mathbf{u}_μ , \mathbf{u}_ν , and \mathbf{R} , but are independent of the distance \mathbf{R} between the two plaquettes. Ref. [48] also separately studied the correlators precisely at the RK point (which sits at the phase boundary between deconfined and confined phases) where the effective field theory differs from the regular Maxwell theory. In the RK wavefunction, while the behavior of the plaquette correlators differs from Eq. (50), it is still a power law with a slower decay [48]. We note that, if the experimentally prepared state is close to an RK wavefunction (see discussion in Sec. III C), then this distinction will be important.

Outside of the deconfined phase (QSL) of the compact $U(1)$ gauge theory, Maxwell electromagnetism is no longer the effective theory, and the behavior of the correlators is different. The ice ferromagnet state is an ordered state with the spins pointing in the z -direction, thus the two plaquette correlators are expected to decay exponentially with \mathbf{R} . The TFP phase has $\langle \hat{S}^+ \rangle \neq 0$, and hence the plaquette X correlator approaches a nonzero constant at large \mathbf{R} , while the plaquette Y correlator is 0 (or decays exponentially or faster in \mathbf{R}). Lastly, in a classical spin liquid, which consists of an incoherent mixture of exponentially many dimer coverings, the plaquette correlators decay at least exponentially (see Table II).

Since the plaquette correlators involve off-diagonal operators, they cannot be read out directly from the snapshots of a Rydberg-atom array. However, we show that they can be measured by evolving the system under a modified Hamiltonian for a specific time duration followed by measurement of a diagonal operator [26, 37]. We describe the protocols to measure both plaquette X and plaquette Y correlators in the sections below.

Correlator	Confined (Ice FM)	Deconfined (QSL)	Higgs (TFP)	Classical Spin Ice
$\langle \hat{X}_P \hat{X}_{P'} \rangle - 4$	Exp. or faster decay	$1/R^8$	Nonzero const.	Exp. or faster decay
$\langle \hat{Y}_P \hat{Y}_{P'} \rangle$	Exp. or faster decay	$1/R^4$	Exp. or faster decay	Exp. or faster decay
$\langle \hat{M}^\dagger \hat{M}(\mathbf{r}_1 \rightarrow \mathbf{r}_2) \rangle$	Nonzero const.	Exp. decay	Exp. decay	Exp. or faster decay
χ_C^E	Nonzero const. ^a	Exp. or faster decay	Nonzero const.	Exp. or faster decay
χ_C^M	Nonzero const.	Exp. or faster decay	Nonzero const. ^a	Exp. or faster decay
$\langle \hat{S}_{ri}^z \hat{S}_{r'j}^z \rangle$	Nonzero const.	$1/R^4$	Exp. decay	$1/R^4$

^a Distinguishing this non-zero constant from zero for χ_C^E in the confined phase (Ice FM) and for χ_C^M in the Higgs phase (TFP) may be practically challenging.

Table II: Behavior of various correlators. \hat{X}_P and \hat{Y}_P are plaquette operators defined in Eq. (47). $\hat{M}^\dagger \hat{M}(\mathbf{r}_1 \rightarrow \mathbf{r}_2)$ is a monopole string operator defined in Eq. (53). χ_C^E and χ_C^M are BFFM order parameters defined in Eq. (60) and Eq. (64), respectively. In this table, we have omitted the form factors multiplying $1/R^4$ and $1/R^8$ that are provided in Eqs. (50) and (65).

1. Plaquette X correlator

For a state $|\Psi_0\rangle$ completely within the ice manifold, the expectation value of $\hat{X}_P \hat{X}_{P'}$ is the same as that of a product of \hat{S}^x operators on the 12 sites of P and P' , that is,

$$\langle \Psi_0 | \hat{X}_P \hat{X}_{P'} | \Psi_0 \rangle = \langle \Psi_0 | \prod_{i=1}^{12} 2\hat{S}_i^x | \Psi_0 \rangle, \quad (51)$$

where the sites $i = 1, 2, \dots, 6$ are on the plaquette P and sites $i = 7, 8, \dots, 12$ are on the plaquette P' . This can be seen by writing $2\hat{S}_i^x = \hat{S}_i^+ + \hat{S}_i^-$ and noticing that the only terms that preserve the ice rule are ring exchanges over P and P' . When the remaining terms act on a state in the ice manifold, they either take the state outside of the ice manifold or annihilate it. Thus the expectation value of these remaining operators in $|\Psi_0\rangle$ is zero. For example, $\hat{S}_1^+ \hat{S}_2^+ \hat{S}_3^+ \hat{S}_4^+ \hat{S}_5^- \hat{S}_6^- \hat{S}_7^+ \hat{S}_8^- \hat{S}_9^+ \hat{S}_{10}^- \hat{S}_{11}^+ \hat{S}_{12}^-$ acting on a state in the ice manifold would either annihilate this state or give a state that violates the ice rule on four of the tetrahedra surrounding P . The protocol to measure the plaquette X correlator is as follows.

We abruptly change the phase and the amplitude of the Rabi frequency, so that the new Hamiltonian is $\hat{H}_Y \approx \Omega_Y \sum_i \hat{S}_i^y$ with $\Omega_Y \gg V$. (Achieving $\Omega_Y \gg V$ may require working with atom spacings that are sufficiently large and/or with Rydberg principal quantum numbers that are sufficiently low, but not low enough to make Rydberg lifetime a problem.) It is assumed that this change of the Hamiltonian is done sufficiently rapidly so that the sudden approximation is valid and the state of the system does not change. We evolve the system under \hat{H}_Y for a time $t_Y = \pi/(2\Omega_Y)$, which amounts to a $\pi/2$ pulse about the y -axis, and then measure all atoms in the $\{|g\rangle, |r\rangle\}$ basis. Thanks to Eq. (51), this allows us to compute the plaquette X correlator.

Eq. (51) assumes that the state $|\Psi_0\rangle$ is in the ice manifold. However, the ground state $|\Psi_g\rangle$ of the system is not completely in the ice manifold. The error introduced because of assuming $|\Psi_g\rangle$ to be in the ice manifold is

of sixth order in Ω/V , as we show in Appendix B. The intuitive reason for this is that six factors of \hat{H}_Ω are required to give a state that can have nonzero overlap with $\prod_{i=1}^{12} 2\hat{S}_i^x |\Psi_0\rangle$.

We note that, for $\Omega/V \gg 1$ (i.e. in the TFP phase), the experimentally measured quantity $\langle \Psi_g | \prod_{i=1}^{12} 2\hat{S}_i^x | \Psi_g \rangle$ is not the same as the plaquette X correlator $\langle \Psi_0 | \hat{X}_P \hat{X}_{P'} | \Psi_0 \rangle$, but their behaviors are nevertheless the same, i.e., both approach a nonzero constant as the distance between the plaquettes increases.

The plaquette X correlator behaves as $\langle \hat{X}_P \hat{X}_{P'} \rangle - 4 \propto 1/R^8$ (the angular dependence is not shown here) in the QSL phase. Although it is a power law, the decay is very rapid, and it might be practically difficult to distinguish it from an exponential decay. This issue is less prominent in the plaquette Y correlator, and we now provide a protocol to measure it.

2. Plaquette Y correlator

This protocol relies on the fact that, for a state $|\Psi_0\rangle$ within the ice manifold, we have an identity similar to Eq. (51):

$$\langle \Psi_0 | \hat{Y}_P \hat{Y}_{P'} | \Psi_0 \rangle = \langle \Psi_0 | \prod_{i=1}^6 (2\hat{S}_{2i-1}^x)(2\hat{S}_{2i}^y) | \Psi_0 \rangle. \quad (52)$$

Recall that sites $1, 2, \dots, 6$ are on P , while sites $7, 8, \dots, 12$ are on P' . This protocol is the same as the protocol for measuring the plaquette X correlator, except that now the $\pi/2$ pulses on sites $2i$ for $i = 1, 2, \dots, 6$ are about the x -axis on the Bloch sphere while the $\pi/2$ pulses on sites $2i-1$ for $i = 1, 2, \dots, 6$ are around the y -axis. After applying these $\pi/2$ pulses, $\prod_{i=1}^{12} 2\hat{S}_i^z$ is measured by taking a snapshot of the array. Note that, for any set of non-overlapping plaquettes, we can simultaneously measure Y correlators between all pairs of plaquettes in this set.

This protocol requires control over individual sites and has an error of order $(\Omega/V)^6$ (the estimation of the er-

ror is similar to the one for the plaquette X correlator done in Appendix B). The advantage of the plaquette Y correlator over the plaquette X correlator is that the former decays as $1/R^4$, which is slower than the decay of the plaquette X correlator and can be easier to observe experimentally.

B. Monopole-monopole correlator

In the deconfined phase, monopoles are gapped. Therefore, the expectation value of an (equal-time) operator that creates a string with a monopole and an antimonopole at its endpoints should decay exponentially with the length of the string. On the other hand, in the confined phase, monopoles are condensed, and hence the expectation value should approach a nonzero constant as the length of the string increases. In the continuum, the following operator inserts a string that creates a monopole at \mathbf{r}_1 and an antimonopole at \mathbf{r}_2 [48]:

$$\hat{\mathcal{M}}^\dagger \hat{\mathcal{M}}(\mathbf{r}_1 \rightarrow \mathbf{r}_2) \sim e^{i \int d^3 \mathbf{r}' \mathcal{A}(\mathbf{r}') \cdot \hat{\mathbf{e}}(\mathbf{r}')} \quad (53)$$

Here $\mathcal{A}(\mathbf{r}')$ is a classical (non single-valued) vector potential such that the flux ϕ_Σ of $\mathcal{B} = \nabla \times \mathcal{A}$ through a closed surface Σ is

$$\phi_\Sigma \equiv \oint_\Sigma \mathcal{B} \cdot d\mathbf{S} = 2\pi q Q_\Sigma, \quad (54)$$

where $Q_\Sigma = 1$ when Σ encloses \mathbf{r}_1 and not \mathbf{r}_2 , $Q_\Sigma = -1$ when Σ encloses \mathbf{r}_2 and not \mathbf{r}_1 , and $Q_\Sigma = 0$ otherwise. q is an integer and denotes the “charge” of the monopole string. For simplicity, we will set $q = 1$ in this section. We clarify that \mathcal{B} and ϕ_Σ are classical numbers and are different from $\hat{\mathbf{b}}$ and $\hat{\Phi}_\Sigma$ which are operators. $\hat{\mathbf{b}} \equiv \nabla \times \hat{\mathbf{a}}$, for gauge-field (operator) $\hat{\mathbf{a}}$, and $\hat{\Phi}_\Sigma$ is defined as

$$\hat{\Phi}_\Sigma \equiv \oint_\Sigma \hat{\mathbf{b}} \cdot d\mathbf{S} = 2\pi \hat{m}, \quad (55)$$

where \hat{m} takes integer eigenvalues. The form of the monopole string operator is chosen so that it increases the flux through Σ by $2\pi Q_\Sigma$, i.e.,

$$[\hat{\Phi}_\Sigma, \hat{\mathcal{M}}^\dagger \hat{\mathcal{M}}(\mathbf{r}_1 \rightarrow \mathbf{r}_2)] = 2\pi Q_\Sigma \hat{\mathcal{M}}^\dagger \hat{\mathcal{M}}(\mathbf{r}_1 \rightarrow \mathbf{r}_2). \quad (56)$$

We now adapt this operator to the Rydberg setting. Consider the diamond lattice formed by the centers of tetrahedra of the pyrochlore lattice, Fig. 1(b). Unlike the continuum, it is now important to specify that the endpoints of the monopole string \mathbf{r}_1 and \mathbf{r}_2 belong to the dual diamond lattice [see Fig. 1(c)], whose sites are centers of “polyhedra” made of four puckered-hexagonal “plaquettes” of the diamond lattice², see Fig. 12(a). Let

² In terms of the original pyrochlore lattice, the vertices of the dual diamond lattice are centers of the truncated tetrahedra [see Fig. 12(b)] which fill the voids between the tetrahedra.

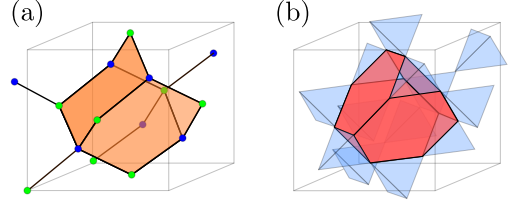


Figure 12: (a) The “polyhedron” formed by four puckered hexagons of the diamond lattice is shown in orange. The centers of these “polyhedra” form the dual diamond lattice. (b) The center of the “polyhedron” in (a) is also the center of a truncated tetrahedron (shown in red) of the pyrochlore lattice.

$\mathbf{x} \equiv \mathbf{r} + \mathbf{e}_\mu/2$ be a site on the pyrochlore lattice, where \mathbf{r} is an A-site of the diamond lattice. $\mathcal{A}_\mathbf{x} \equiv \mathcal{A}_{\mathbf{r}, \mathbf{r} + \mathbf{e}_\mu}$ is the discrete version of \mathcal{A} integrated (Fig. 1(b)) shows the vectors \mathbf{e}_μ along the line pointing from the center of an A tetrahedron (centred at \mathbf{r}) to the B tetrahedron (centred at $\mathbf{r} + \mathbf{e}_\mu$) such that the two tetrahedra touch at \mathbf{x} .

$\mathcal{A}_\mathbf{x}$ is required to satisfy the discrete version of Eq. (54), and hence depends on \mathbf{r}_1 , \mathbf{r}_2 , the “magnetic field” configuration \mathcal{B} and the gauge choice for $\mathcal{A}_\mathbf{x}$. For the pyrochlore lattice, we have

$$\hat{\mathcal{M}}^\dagger \hat{\mathcal{M}}(\mathbf{r}_1 \rightarrow \mathbf{r}_2) = e^{i \sum_{\mathbf{x} \in \text{pyrochlore}} \mathcal{A}_\mathbf{x} (\hat{n}_\mathbf{x} - 1/2)}. \quad (57)$$

This operator is purely diagonal in the $\hat{n}_\mathbf{x}$ basis (i.e., in the \hat{S}^z -basis). So, experimentally, one can calculate this phase for each snapshot and average over shots.

Theoretically, one expects

$$\left| \langle \hat{\mathcal{M}}^\dagger \hat{\mathcal{M}}(\mathbf{r}_1 \rightarrow \mathbf{r}_2) \rangle \right| \sim \begin{cases} e^{-|\mathbf{r}_2 - \mathbf{r}_1|/\lambda}, & \text{deconfined phase,} \\ \text{constant,} & \text{confined phase,} \end{cases} \quad (58)$$

where λ is a correlation length that depends on the monopole gap and the “photon” velocity. In Fig. 13, we provide an example of one configuration of the classical numbers $\mathcal{A}_\mathbf{x}$ that defines a monopole string operator. Below, we comment on the freedom in choosing $\mathcal{A}_\mathbf{x}$.

1. Choice of \mathcal{A}

The classical numbers $\mathcal{A}_\mathbf{x}$ should of course obey the constraint that the flux of $\nabla \times \mathcal{A}$ through a closed surface Σ is $2\pi Q_\Sigma$, as mentioned above. However, one still has a freedom in the choice of \mathcal{A} in the following two respects:

1. Freedom in the arrangement of the field lines of $\nabla \times \mathcal{A}$. For example, they can be confined to a thin tube connecting \mathbf{r}_1 and \mathbf{r}_2 , or be spread out according to Coulomb’s law, or be something in between. Different such arrangements, due to their different energy costs, would differ in sub-leading corrections to the exponentially decaying behavior,

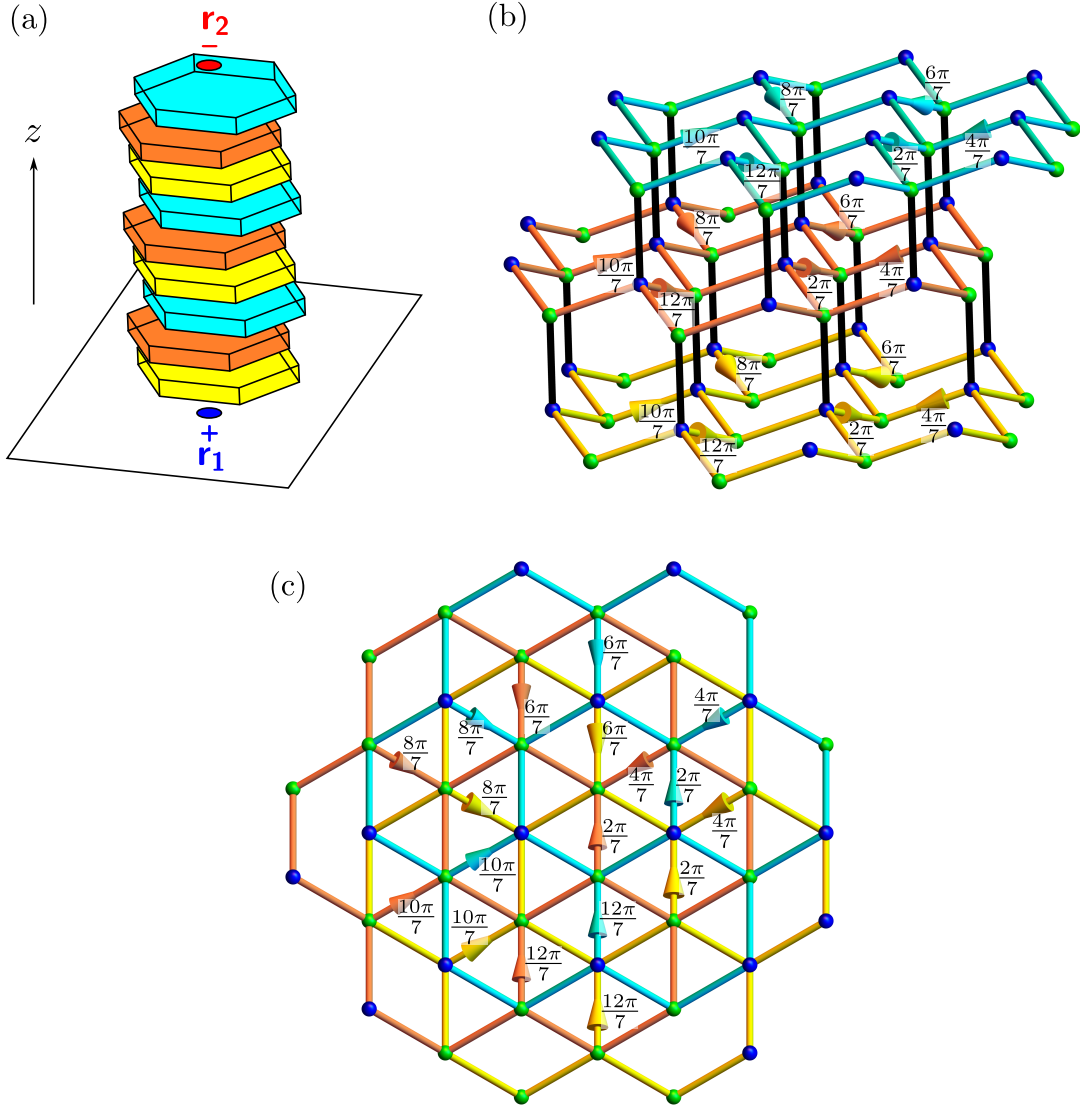


Figure 13: An example of the monopole string operator $\hat{\mathcal{M}}^\dagger \hat{\mathcal{M}}(\mathbf{r}_1 \rightarrow \mathbf{r}_2)$ for which we provide \mathcal{A}_x explicitly. In our example, the string carries 2π flux through a tube with a width of 7 puckered hexagons of the diamond lattice. (a) A schematic of the tube running along the z -direction. The diamond lattice (whose vertices are centers of tetrahedra of the pyrochlore lattice) can be seen as ABC stacking of layers of “honeycomb” lattices made of chair-like puckered hexagons. The tube consists of three types of layers shown in yellow, orange, and cyan. Each layer is made of 7 puckered hexagons. To convey a sketch, we depict such a layer by a big hexagon with some thickness. (b) A side view of the stack showing three of its layers, which then need to be repeated in the z direction to get the entire string. For bonds x with arrows, the value of \mathcal{A}_x is written next to the bond. For bonds x without arrows, $\mathcal{A}_x = 0$. (c) Top view of three of the layers of the stack. It can be seen from all three sub-figures (a)-(c) that the flux through any closed surface Σ that completely encloses an integer number of layers, such that the bottom layer is included but not the top, is 2π . However, if Σ partially encloses a layer, then Φ_Σ is 0. This difficulty in defining arbitrary integer multiples of 2π flux through a volume enclosed by a finite number of plaquettes has been observed before [48]. Therefore in our construction, \mathbf{r}_1 and \mathbf{r}_2 have to be seen as being smeared across 7 points of the dual diamond lattice below the bottom layer and above the top layer respectively, in order to be consistent with Eq. (54).

but the leading behavior would be unchanged. In Fig. 13, we provide a choice of \mathcal{A} , such that the monopole string is localized to a thin tube.

2. For a fixed choice of field lines, we still have a

gauge choice for \mathcal{A} . Consider a gauge transformation $\mathcal{A}_{\mathbf{r}, \mathbf{r} + \mathbf{e}_\mu} \rightarrow \mathcal{A}_{\mathbf{r}, \mathbf{r} + \mathbf{e}_\mu} + \lambda_{\mathbf{r} + \mathbf{e}_\mu} - \lambda_{\mathbf{r}}$, where $\lambda_{\mathbf{r}}$ is

an \mathbf{r} -dependent real number. It results in

$$\hat{\mathcal{M}}^\dagger \hat{\mathcal{M}}(\mathbf{r}_1 \rightarrow \mathbf{r}_2) \rightarrow \hat{\mathcal{M}}^\dagger \hat{\mathcal{M}}(\mathbf{r}_1 \rightarrow \mathbf{r}_2) e^{-i \sum_{\mathbf{r}} \lambda_{\mathbf{r}} \eta_{\mathbf{r}} (\hat{n}_{\mathbf{r}} - 2)}, \quad (59)$$

where $\eta_{\mathbf{r}} = 1$ for $\mathbf{r} \in A$ and $\eta_{\mathbf{r}} = -1$ for $\mathbf{r} \in B$. In the $\Omega/V \ll 1$ limit, we have $\hat{n}_{\Delta_{\mathbf{r}}} = 2$, so the expectation value is invariant under the gauge transformation. Away from this limit, a gauge transformation on $\mathcal{A}_{\mathbf{r}, \mathbf{r} + \mathbf{e}_\mu}$ generically results in a physical transformation on the monopole string operator. However, as long as the external field $h = 0$ [h is defined in Eq. (5)], by particle-hole symmetry, we have $\langle \hat{n}_{\Delta_{\mathbf{r}}} \rangle = 2$, and $\langle (\hat{n}_{\Delta_{\mathbf{r}}} - 2)^2 \rangle$ is bounded. Hence we do not expect the gauge transformation on $\mathcal{A}_{\mathbf{r}, \mathbf{r} + \mathbf{e}_\mu}$ to qualitatively change the behavior of Eq. (58).

C. BFFM order parameter

It is known that the confined and deconfined phases of a gauge theory without matter fields can be distinguished by the scaling of the Wilson loops $W_{\mathcal{L}} = \langle e^{i \oint_{\mathcal{L}} A_\mu dx^\mu} \rangle$, where A_μ is the gauge field and \mathcal{L} is a closed loop. In the deconfined phase, the Wilson loop follows the perimeter law, $W_{\mathcal{L}} \propto e^{-\text{Perimeter of } \mathcal{L}}$, while in the confined phase, it follows the area law, $W_{\mathcal{L}} \propto e^{-\text{Area of } \mathcal{L}}$. However, in the presence of matter fields (which are generically always present), the Wilson loop follows the perimeter law in both phases [86, 87], and it cannot be used to distinguish them. The Bricmont-Fröhlich-Fredenhagen-Marcu (BFFM) order parameter is useful in such cases and has a different behavior in the two phases [26, 37, 88–93]. The BFFM order parameter, denoted here by $\chi_{\mathcal{C}}^E$, is defined as

$$\chi_{\mathcal{C}}^E = \frac{|\langle e^{i \sum_{\mathcal{C}} \hat{a}_{\mathbf{r}\mathbf{r}'} + \text{H.c.}} \rangle|}{\sqrt{|\langle e^{i \sum_{\mathcal{L}} \hat{a}_{\mathbf{r}\mathbf{r}'} + \text{H.c.}} \rangle|}}, \quad (60)$$

where \mathcal{C} is an open curve and \mathcal{L} is the closed loop formed by combining \mathcal{C} with its mirror image about a plane that intersects \mathcal{C} only at its end points. This order parameter detects long-range order in the “electric charge”-creation string. In the Higgs phase, “electric charges” are condensed, and hence $\chi_{\mathcal{C}}^E$ approaches a nonzero constant. In the deconfined phase, the numerator in Eq. (60) (calculated on an open curve) decays to zero faster than the denominator (calculated on a closed loop, giving the Wilson loop), as the length of \mathcal{C} is increased. Therefore, in the deconfined phase, $\chi_{\mathcal{C}}^E$ goes to 0 as the length of \mathcal{C} is increased. In the confined phase, it was argued in Ref. [89] that while both the numerator and the denominator go to zero as the length of \mathcal{C} is increased, the limit of their ratio approaches a constant. However distinguishing this constant from zero in finite systems for finite length of \mathcal{C} may be difficult. Below we explain how to measure $\chi_{\mathcal{C}}^E$.

Using the mapping from spin operators to gauge fields,

Eqs. (13) and (15), we see that

$$e^{i \sum_{\mathcal{C}} \hat{a}_{\mathbf{r}\mathbf{r}'}} \simeq \hat{S}_1^+ \hat{S}_2^- \hat{S}_3^+ \dots, \quad (61)$$

where the product of \hat{S}^+ and \hat{S}^- operators is over the sites on the curve \mathcal{C} . The denominator in $\chi_{\mathcal{C}}^E$ has a similar expression in terms of spin operators.

From the point of view of measurement, it is more convenient to consider another quantity, which has the same behavior as $\chi_{\mathcal{C}}^E$ in the three phases, defined as:

$$\tilde{\chi}_{\mathcal{C}}^E \equiv \frac{|\langle \prod_{i \in \mathcal{C}} \hat{S}_i^x \rangle|}{\sqrt{|\langle \prod_{i \in \mathcal{L}} \hat{S}_i^x \rangle|}}, \quad (62)$$

In the transverse-field-polarized (Higgs) phase, $\tilde{\chi}_{\mathcal{C}}^E$ approaches a nonzero constant, just like $\chi_{\mathcal{C}}^E$. Now, we argue that even in the QSL and confined phases, $\tilde{\chi}_{\mathcal{C}}^E$ and $\chi_{\mathcal{C}}^E$ have the same behavior. For a state $|\Psi\rangle$ that dominantly lies in the ice manifold, with corrections from outside the ice manifold being of order Ω/V (such as the ground state $|\Psi_g\rangle$), we have

$$\begin{aligned} \langle \Psi | \hat{S}_1^+ \hat{S}_2^- \hat{S}_3^+ \dots + \text{H.c.} | \Psi \rangle \\ = \langle \Psi | (2\hat{S}_1^x)(2\hat{S}_2^x)(2\hat{S}_3^x) \dots | \Psi \rangle + \Theta((\Omega/V)^L), \end{aligned} \quad (63)$$

where L is the number of sites on \mathcal{C} . The correction is of order $(\Omega/V)^L$ by an argument similar to the one used to show that the error is sixth order in the protocol to measure the plaquette X correlator (see Appendix B). Thus, for small Ω/V , $\chi_{\mathcal{C}}^E$ and $\tilde{\chi}_{\mathcal{C}}^E$ are equal up to order $(\Omega/V)^L$.

The numerator and the denominator of $\tilde{\chi}_{\mathcal{C}}^E$ can be measured by applying $\pi/2$ pulses about the y -axis and measuring, from the snapshots, products of \hat{S}^z along \mathcal{C} and \mathcal{L} . This procedure is similar to the protocol to measure the plaquette X correlator, described in Sec. IV A 1.

The operator $e^{i \sum_{\mathcal{C}} \hat{a}_{\mathbf{r}\mathbf{r}'}}$ creates two opposite “electric charges” at the endpoints of \mathcal{C} . So a magnetic analogue of $\chi_{\mathcal{C}}^E$ can also be defined, where the numerator is the expectation value of the operator that creates a monopole and an antimonopole at the endpoints of \mathcal{C} . Such an order parameter, $\chi_{\mathcal{C}}^M$, detects long-range order in the monopole string operator and is given by

$$\chi_{\mathcal{C}}^M = \frac{\langle \hat{\mathcal{M}}^\dagger \hat{\mathcal{M}}(\mathbf{r}_1 \xrightarrow{\mathcal{C}} \mathbf{r}_2) \rangle}{\sqrt{\langle \hat{\mathcal{M}}^\dagger \hat{\mathcal{M}}(\mathbf{r}_1 \xrightarrow{\mathcal{L}} \mathbf{r}_1) \rangle}}, \quad (64)$$

where $\hat{\mathcal{M}}^\dagger \hat{\mathcal{M}}(\mathbf{r}_1 \xrightarrow{\mathcal{C}} \mathbf{r}_2)$ inserts a monopole-antimonopole string along \mathcal{C} and was defined in Eq. (57). In this section, we use the notation where the path of the monopole-antimonopole string is explicitly written in the argument of $\hat{\mathcal{M}}^\dagger \hat{\mathcal{M}}$. Since this operator is diagonal in the \hat{S}^z basis, it can be measured straightforwardly from the snapshots of the Rydberg-atom array.

In the confined phase, monopoles are condensed, so $\chi_{\mathcal{C}}^M$ should be a nonzero constant. In the deconfined phase, by the argument of Ref. [89], the numerator of Eq. (64) decays to zero faster than the denominator as the length of \mathcal{C} increases. Therefore, in the deconfined phase, $\chi_{\mathcal{C}}^M$ goes to zero as the length of \mathcal{C} increases. In the Higgs phase, even though there is no long-range order in the monopole string and both the numerator and denominator go to zero, by the argument in Ref. [89], the ratio (i.e. $\chi_{\mathcal{C}}^M$) approaches a nonzero constant as the length of \mathcal{C} increases. But distinguishing this non-zero constant from zero in finite-size numerics and experiment may be challenging (similar to the situation for $\chi_{\mathcal{C}}^E$ in the confined phase).

The behavior of the BFFM order parameters in various phases is summarized in Table II.

Before proceeding, we note that our protocols to measure the plaquette correlators and the BFFM order parameter $\chi_{\mathcal{C}}^E$ work in the limit $\Omega/V \ll 1$, which is outside the window in which the ground state of Hamiltonian (6) is a QSL. However, we explained in Sec. III C that it is possible to dynamically prepare finite puddles of QSL regions even in the $\Omega/V \ll 1$ limit when the ground state is not a QSL. Our protocols can then be applicable.

D. Two-point \hat{S}^z correlator

Consider two spins $\hat{S}_{\mathbf{r},\mu}^z$ and $\hat{S}_{\mathbf{r}',\nu}^z$ located on the sites $\mathbf{r} + \mathbf{e}_\mu/2$ and $\mathbf{r}' + \mathbf{e}_\nu/2$, where \mathbf{r} and \mathbf{r}' are the centers of two up-pointing tetrahedra and $\mu, \nu \in \{0, 1, 2, 3\}$ label the sites of the tetrahedra (see Fig. 14). From the mapping of spins to gauge theory, Eqs. (13) and (15), it can be seen that the two-point correlator of these two spins $\langle \hat{S}_{\mathbf{r},\mu}^z \hat{S}_{\mathbf{r}',\nu}^z \rangle$ is the same as the two-point correlator of the electric field.

The effective theory in the deconfined phase is the Maxwell electromagnetism. In the $3 + 1$ D continuum Maxwell electromagnetism, the correlator of the Cartesian components of the electric field $\hat{e}_{\mathbf{r},i}$ for $i \in \{x, y, z\}$ can be expressed as Gaussian integral which evaluate to [48]

$$\langle \hat{e}_{\mathbf{0},i} \hat{e}_{\mathbf{R},j} \rangle_0 \propto \frac{1}{R^4} \left(2 \frac{R_i R_j}{R^2} - \delta_{ij} \right), \quad (65)$$

where $\langle \cdot \rangle_0$ denotes expectation value with respect to the Maxwell action.

The correlator of the electric field operators $\hat{e}_{\mathbf{r},\mu}$ for $\mu \in \{0, 1, 2, 3\}$ along the links of the diamond lattice are obtained from Eq. (65) by taking components of the Cartesian electric field along the vectors \mathbf{e}_μ . The result is

$$\langle \hat{S}_{\mathbf{r},\mu}^z \hat{S}_{\mathbf{r}',\nu}^z \rangle = \sum_{k,l \in \{x,y,z\}} (\mathbf{e}_\mu)_k (\mathbf{e}_\nu)_l \langle \hat{e}_{\mathbf{r},k} \hat{e}_{\mathbf{r}',l} \rangle_0, \quad (66)$$

In the confined phase (ice ferromagnet), which is primarily diagonal in the \hat{S}^z basis, this correlator should

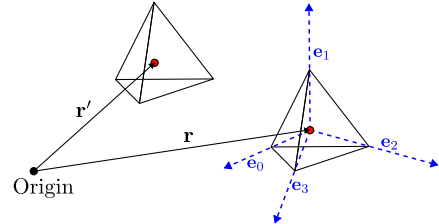


Figure 14: Notation for the two-point \hat{S}^z correlator. \mathbf{r} and \mathbf{r}' are the positions of the centers of the tetrahedra. \mathbf{e}_μ are the vectors joining the center of an up-pointing tetrahedron to the centers of its neighboring down-pointing tetrahedra.

approach a constant for large $R = |\mathbf{r} - \mathbf{r}'|$. On the other hand, in the TFP phase, which is primarily a product state in the \hat{S}^x basis, this correlator decays at least exponentially with R (see Table II). Since $\hat{S}_{\mathbf{r},\mu}^z \hat{S}_{\mathbf{r}',\nu}^z$ is a diagonal operator, its correlator can be measured experimentally by capturing snapshots of the Rydberg-atom array and averaging over them.

V. DISCUSSION

In this work, we have presented a proposal to prepare and detect the deconfined phase of the $U(1)$ gauge theory in $3+1$ dimensions on a Rydberg atom simulator. We first showed that laser-driven neutral atoms trapped in a pyrochlore lattice using optical tweezer arrays naturally realize a $U(1)$ quantum spin liquid as the ground state when the laser detuning lies in a specified window and the interactions between Rydberg atoms are restricted to nearest-neighbor. We then studied the effect of van der Waals interactions beyond nearest-neighbor. In the classical limit obtained by dropping the Rabi frequency term, we showed that long-range interactions break the degeneracy to select an ice ferromagnet as the ground state. We then studied the competition between the long-ranged interactions that prefer an ordered state and quantum fluctuations that prefer a QSL state, by calculating the energies in ansatz wavefunctions using perturbation theory. We found that, for Rabi frequencies greater than $\Omega_C \approx 0.44V$, the ground state is a QSL within our approximation. When Ω is increased further, we argued that the QSL goes into a transverse-field-polarized state via a Higgs transition. While we have focused on the ground state, we also commented on the effect of dynamical state preparation in deciding the nature of the prepared state. We then provided experimental protocols for measuring the plaquette correlators, Bricmont-Fröhlich-Fredenhagen-Marcu order parameters, the monopole-monopole correlator, and the “electric field” correlator that can distinguish a QSL phase from ordered phases.

Our ground state phase diagram is the result of an approximate calculation. While it is possible that the

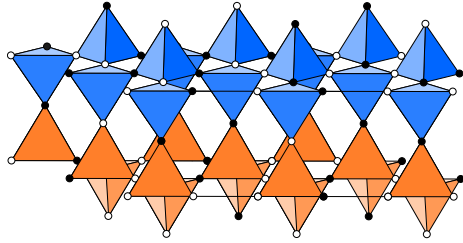


Figure 15: A lattice made of corner-sharing tetrahedra different from the pyrochlore lattice. The lattice consists of $ABAB\dots$ stacking of the blue (A) and the orange (B) layers. A configuration satisfying $n_{\Delta} = 2$ is shown here.

true phase diagram differs from what we found, we note that there are other knobs one can tune to get a desired phase diagram. Dressed states created from multiple Rydberg and possibly ground levels can be used to customize the interactions away from the isotropic $1/r^6$ form we considered in this paper [94–99]. Designing a dressing scheme compatible with the symmetries of the pyrochlore lattice and exploring the resulting phase diagrams is an interesting direction for future work. We also note that our proposal requires two Rydberg excitations per tetrahedron, meaning that it lies outside of the Rydberg-blockade regime and is therefore sensitive to imperfections and thermal fluctuations in nearest-neighbor spacing. It will therefore be useful to extend our proposal to the blockade regime of one excitation per tetrahedron. While previous numerical work on dimer models have required a nonzero RK potential (6-body term) to achieve this, it will be worthwhile to study if one can engineer long-range Rydberg interactions that stabilize a spin-liquid in the blockade regime.

One can also look for other lattices that could realize a $U(1)$ QSL ground state. One such possibility is a lattice of corner-sharing tetrahedra where all up-pointing tetrahedra (and separately all down-pointing tetrahedra) form a hexagonal close-packed lattice shown in Fig. 15. If only nearest-neighbor interactions are considered between atoms positioned on the sites of this lattice, then, by perturbation theory in Ω/V for a particular range of detunings, one gets ring exchange terms similar to the ones obtained in Sec. II A, and the system maps onto a dimer model. It is not known if this dimer model is in the QSL phase when the RK potential is zero and long range van der Waals interactions are included. Another open problem is to construct lattices where a dimer model can

be realized within the blockade regime without the RK potential.

Next, we note that, formally, a distinction between the confined and deconfined phases exists only in the thermodynamic limit. Experimentally, there are two finiteness effects that can be important. First, a realistic three dimensional Rydberg array will likely have a relatively small linear dimension. Some of the correlators presented in Sec. IV require asymptotic behavior in distance to distinguish different phases. Second, as found in Ref. [81] and mentioned in Sec. III C, a finite-time state preparation scheme would generically prepare puddles of spin-liquid regions as opposed to an entire spin liquid. It is therefore necessary to quantitatively study how the behavior of the correlators is modified under these conditions.

We also note that, to translate field-theory observables into microscopic variables, we relied on the perturbative limit of small Ω/V . However in the phase diagram that we found, the region where the spin liquid is a ground state does not satisfy $\Omega/V \ll 1$. Understanding how the field-theory operators (e.g. plaquette, monopole, and electric-field operators) get renormalized away from the perturbative limit is important both from fundamental and practical standpoints.

Our work is a proposal to prepare a gapless $U(1)$ spin liquid using unitary evolution. An interesting research direction would be to come up with schemes that also use projective measurements to expedite the state preparation along the lines of Refs. [44, 100]. One can also explore how other exotic phases of matter such as fractons and 3+1D topological order can potentially be realized on a Rydberg simulator.

ACKNOWLEDGMENTS

We thank Nikita Astrakhantsev, Peter Lunts, Nathan Schine, Alexander Schuckert, Dayal Singh, and Ashvin Vishwanath for discussions. J.S., G.N., and V.G. were supported by NSF DMR-2037158, US-ARO Contract No.W911NF1310172, and Simons Foundation. J.S. and A.V.G. were supported in part by AFOSR, NSF QLCI (award No. OMA-2120757), DoE QSA, DoE ASCR Accelerated Research in Quantum Computing program (award No. DE-SC0020312), the DoE ASCR Quantum Testbed Pathfinder program (award No. DE-SC0019040), NSF PFCQC program, ARO MURI, AFOSR MURI, and DARPA SAVaNT ADVENT.

[1] P. W. Anderson, Resonating valence bonds: A new kind of insulator?, *Mater. Res. Bulletin* **8**, 153 (1973).

[2] L. Savary and L. Balents, Quantum spin liquids: A review, *Rep. Prog. Phys.* **80**, 016502 (2017).

[3] T. Senthil, A. Vishwanath, L. Balents, S. Sachdev, and M. P. Fisher, Deconfined quantum critical points, *Science* **303**, 1490 (2004).

[4] M. Hermele, T. Senthil, and M. P. Fisher, Algebraic spin liquid as the mother of many competing orders, *Physical Review B* **72**, 104404 (2005).

[5] X.-Y. Song, C. Wang, A. Vishwanath, and Y.-C. He, Unifying description of competing orders in two-

dimensional quantum magnets, *Nature communications* **10**, 1 (2019).

[6] G. Nambiar, D. Bulmash, and V. Galitski, Monopole josephson effects in a dirac spin liquid (2022).

[7] W. Marciano and H. Pagels, Quantum chromodynamics, *Phys. Rep.* **36**, 137 (1978).

[8] H. Meyer-Ortmanns, Phase transitions in quantum chromodynamics, *Rev. Mod. Phys.* **68**, 473 (1996).

[9] J. B. Kogut, The lattice gauge theory approach to quantum chromodynamics, *Rev. Mod. Phys.* **55**, 775 (1983).

[10] L. O’Raifeartaigh and N. Straumann, Gauge theory: Historical origins and some modern developments, *Rev. Mod. Phys.* **72**, 1 (2000).

[11] P. A. Lee, N. Nagaosa, and X.-G. Wen, Doping a mott insulator: Physics of high-temperature superconductivity, *Rev. Mod. Phys.* **78**, 17 (2006).

[12] A. Y. Kitaev, Fault-tolerant quantum computation by anyons, *Ann. Phys. (N. Y.)* **303**, 2 (2003).

[13] C. Nayak, S. H. Simon, A. Stern, M. Freedman, and S. D. Sarma, Non-abelian anyons and topological quantum computation, *Rev. Mod. Phys.* **80**, 1083 (2008).

[14] J. Knolle and R. Moessner, A field guide to spin liquids, *Annu. Rev. Condens. Matter Phys.* **10**, 451 (2019).

[15] H. Weimer, M. Müller, I. Lesanovsky, P. Zoller, and H. P. Büchler, A rydberg quantum simulator, *Nat. Phys.* **6**, 382 (2010).

[16] S. Ebadi, T. T. Wang, H. Levine, A. Keesling, G. Semeghini, A. Omran, D. Bluvstein, R. Samajdar, H. Pichler, W. W. Ho, *et al.*, Quantum phases of matter on a 256-atom programmable quantum simulator, *Nature* **595**, 227 (2021).

[17] X. Wu, X. Liang, Y. Tian, F. Yang, C. Chen, Y.-C. Liu, M. K. Tey, and L. You, A concise review of rydberg atom based quantum computation and quantum simulation, *Chin. Phys. B* **30**, 020305 (2021).

[18] M. Saffman, T. G. Walker, and K. Mølmer, Quantum information with Rydberg atoms, *Rev. Mod. Phys.* **82**, 2313 (2010).

[19] M. D. Lukin, M. Fleischhauer, R. Cote, L. M. Duan, D. Jaksch, J. I. Cirac, and P. Zoller, Dipole Blockade and Quantum Information Processing in Mesoscopic Atomic Ensembles, *Phys. Rev. Lett.* **87**, 037901 (2001).

[20] H. Labuhn, D. Barredo, S. Ravets, S. de Léséleuc, T. Macrì, T. Lahaye, and A. Browaeys, Tunable two-dimensional arrays of single Rydberg atoms for realizing quantum Ising models, *Nature* **534**, 667 (2016).

[21] D. Jaksch, J. I. Cirac, P. Zoller, S. L. Rolston, R. Côté, and M. D. Lukin, Fast Quantum Gates for Neutral Atoms, *Phys. Rev. Lett.* **85**, 2208 (2000).

[22] A. Browaeys, D. Barredo, and T. Lahaye, Experimental investigations of dipole-dipole interactions between a few Rydberg atoms, *J. Phys. B* **49**, 152001 (2016).

[23] D. Barredo, S. de Léséleuc, V. Lienhard, T. Lahaye, and A. Browaeys, An atom-by-atom assembler of defect-free arbitrary two-dimensional atomic arrays, *Science* **354**, 1021 (2016).

[24] L. Béguin, A. Vernier, R. Chicireanu, T. Lahaye, and A. Browaeys, Direct Measurement of the van der Waals Interaction between Two Rydberg Atoms, *Phys. Rev. Lett.* **110**, 263201 (2013).

[25] D. Barredo, V. Lienhard, S. de Léséleuc, T. Lahaye, and A. Browaeys, Synthetic three-dimensional atomic structures assembled atom by atom, *Nature* **561**, 79 (2018).

[26] G. Semeghini, H. Levine, A. Keesling, S. Ebadi, T. T. Wang, D. Bluvstein, R. Verresen, H. Pichler, M. Kalinowski, R. Samajdar, A. Omran, S. Sachdev, A. Vishwanath, M. Greiner, V. Vuletić, and M. D. Lukin, Probing Topological Spin Liquids on a Programmable Quantum Simulator, *Science* **374**, 1242 (2021).

[27] H. Bernien, S. Schwartz, A. Keesling, H. Levine, A. Omran, H. Pichler, S. Choi, A. S. Zibrov, M. Endres, M. Greiner, V. Vuletić, and M. D. Lukin, Probing many-body dynamics on a 51-atom quantum simulator, *Nature* **551**, 579 (2017).

[28] D. Bluvstein, H. Levine, G. Semeghini, T. T. Wang, S. Ebadi, M. Kalinowski, A. Keesling, N. Maskara, H. Pichler, M. Greiner, V. Vuletić, and M. D. Lukin, A quantum processor based on coherent transport of entangled atom arrays, *Nature* **604**, 451 (2022).

[29] E. Guardado-Sánchez, P. T. Brown, D. Mitra, T. Devakul, D. A. Huse, P. Schauß, and W. S. Bakr, Probing the Quench Dynamics of Antiferromagnetic Correlations in a 2D Quantum Ising Spin System, *Phys. Rev. X* **8**, 021069 (2018).

[30] A. Keesling, A. Omran, H. Levine, H. Bernien, H. Pichler, S. Choi, R. Samajdar, S. Schwartz, P. Silvi, S. Sachdev, P. Zoller, M. Endres, M. Greiner, V. Vuletić, and M. D. Lukin, Quantum Kibble-Zurek mechanism and critical dynamics on a programmable Rydberg simulator, *Nature* **568**, 207 (2019).

[31] H. Levine, A. Keesling, G. Semeghini, A. Omran, T. T. Wang, S. Ebadi, H. Bernien, M. Greiner, V. Vuletić, H. Pichler, and M. D. Lukin, Parallel Implementation of High-Fidelity Multiqubit Gates with Neutral Atoms, *Phys. Rev. Lett.* **123**, 170503 (2019).

[32] V. Lienhard, S. de Léséleuc, D. Barredo, T. Lahaye, A. Browaeys, M. Schuler, L.-P. Henry, and A. M. Läuchli, Observing the Space- and Time-Dependent Growth of Correlations in Dynamically Tuned Synthetic Ising Models with Antiferromagnetic Interactions, *Phys. Rev. X* **8**, 021070 (2018).

[33] I. S. Madjarov, J. P. Covey, A. L. Shaw, J. Choi, A. Kale, A. Cooper, H. Pichler, V. Schkolnik, J. R. Williams, and M. Endres, High-fidelity entanglement and detection of alkaline-earth Rydberg atoms, *Nat. Phys.* **16**, 857 (2020).

[34] A. Omran, H. Levine, A. Keesling, G. Semeghini, T. T. Wang, S. Ebadi, H. Bernien, A. S. Zibrov, H. Pichler, S. Choi, J. Cui, M. Rossignolo, P. Rembold, S. Montangero, T. Calarco, M. Endres, M. Greiner, V. Vuletić, and M. D. Lukin, Generation and manipulation of Schrödinger cat states in Rydberg atom arrays, *Science* **365**, 570 (2019).

[35] P. Schauß, J. Zeiher, T. Fukuhara, S. Hild, M. Cheneau, T. Macrì, T. Pohl, I. Bloch, and C. Gross, Crystallization in Ising quantum magnets, *Science* **347**, 1455 (2015).

[36] Y. Song, M. Kim, H. Hwang, W. Lee, and J. Ahn, Quantum annealing of Cayley-tree Ising spins at small scales, *Phys. Rev. Res.* **3**, 013286 (2021).

[37] R. Verresen, M. D. Lukin, and A. Vishwanath, Prediction of Toric Code Topological Order from Rydberg Blockade, *Phys. Rev. X* **11**, 031005 (2021).

[38] R. Samajdar, W. W. Ho, H. Pichler, M. D. Lukin, and S. Sachdev, Quantum phases of Rydberg atoms on a kagome lattice, *Proc. Natl. Acad. Sci. U.S.A.* **118**, e2015785118 (2021).

[39] N. E. Myerson-Jain, S. Yan, D. Weld, and C. Xu, Con-

struction of fractal order and phase transition with rydberg atoms, *Phys. Rev. Lett.* **128**, 017601 (2022).

[40] K. Slagle, Y. Liu, D. Aasen, H. Pichler, R. S. K. Mong, X. Chen, M. Endres, and J. Alicea, Quantum spin liquids bootstrapped from ising criticality in rydberg arrays, *Phys. Rev. B* **106**, 115122 (2022).

[41] M. Kornjača, R. Samajdar, T. Macrì, N. Gemelke, S.-T. Wang, and F. Liu, Trimer quantum spin liquid in a honeycomb array of rydberg atoms, arXiv preprint arXiv:2211.00653 (2022).

[42] Z. Zhou, Z. Yan, C. Liu, Y. Chen, and X.-F. Zhang, Quantum simulation of two-dimensional u(1) gauge theory in rydberg atom arrays, arXiv preprint arXiv:2212.10863 (2022).

[43] Y.-J. Liu, K. Shtengel, A. Smith, and F. Pollmann, Methods for simulating string-net states and anyons on a digital quantum computer, *PRX Quantum* **3**, 040315 (2022).

[44] N. Tantivasadakarn, R. Verresen, and A. Vishwanath, The shortest route to non-abelian topological order on a quantum processor, arXiv preprint arXiv:2209.03964 (2022).

[45] R. Verresen, N. Tantivasadakarn, and A. Vishwanath, Efficiently preparing ghz, topological and fracton states by measuring cold atoms, arXiv preprint arXiv:2112.03061 (2021).

[46] A. M. Polyakov, Compact gauge fields and the infrared catastrophe, *Phys. Lett. B* **59**, 82 (1975).

[47] A. Polyakov, Quark confinement and topology of gauge theories, *Nucl. Phys. B* **120**, 429 (1977).

[48] M. Hermele, M. P. A. Fisher, and L. Balents, Pyrochlore photons: The U(1) spin liquid in a $S = 1/2$ three-dimensional frustrated magnet, *Phys. Rev. B* **69**, 064404 (2004).

[49] D. A. Huse, W. Krauth, R. Moessner, and S. L. Sondhi, Coulomb and Liquid Dimer Models in Three Dimensions, *Phys. Rev. Lett.* **91**, 167004 (2003).

[50] A. Banerjee, S. V. Isakov, K. Damle, and Y. B. Kim, Unusual Liquid State of Hard-Core Bosons on the Pyrochlore Lattice, *Phys. Rev. Lett.* **100**, 047208 (2008).

[51] N. Shannon, O. Sikora, F. Pollmann, K. Penc, and P. Fulde, Quantum Ice: A Quantum Monte Carlo Study, *Phys. Rev. Lett.* **108**, 067204 (2012).

[52] S. T. Bramwell and M. J. Harris, The history of spin ice, *J. Condens. Matter Phys.* **32**, 374010 (2020).

[53] M. J. Gingras, Spin ice, Introduction to frustrated magnetism , 293 (2011).

[54] M. Udagawa and L. Jaubert, *Spin Ice* (Springer, 2021).

[55] S. H. Skjærvø, C. H. Marrows, R. L. Stamps, and L. J. Heyderman, Advances in artificial spin ice, *Nat. Rev. Phys.* **2**, 13 (2020).

[56] C. Nisoli, R. Moessner, and P. Schiffer, Colloquium: Artificial spin ice: Designing and imaging magnetic frustration, *Rev. Mod. Phys.* **85**, 1473 (2013).

[57] L. Pauling, The Structure and Entropy of Ice and of Other Crystals with Some Randomness of Atomic Arrangement, *J. Am. Chem. Soc.* **57**, 2680 (1935).

[58] M. J. Gingras and P. A. McClarty, Quantum spin ice: a search for gapless quantum spin liquids in pyrochlore magnets, *Rep. Prog. Phys.* **77**, 056501 (2014).

[59] S. Tewari, V. W. Scarola, T. Senthil, and S. D. Sarma, Emergence of artificial photons in an optical lattice, *Phys. Rev. Lett.* **97**, 200401 (2006).

[60] A. W. Glaetzle, M. Dalmonte, R. Nath, I. Rousochatza, R. Moessner, and P. Zoller, Quantum spin-ice and dimer models with rydberg atoms, *Phys. Rev. X* **4**, 041037 (2014).

[61] A. Celi, B. Vermersch, O. Viyuela, H. Pichler, M. D. Lukin, and P. Zoller, Emerging two-dimensional gauge theories in rydberg configurable arrays, *Phys. Rev. X* **10**, 021057 (2020).

[62] P. Emonts and S. Wessel, Monte carlo study of the discontinuous quantum phase transition in the transverse-field ising model on the pyrochlore lattice, *Phys. Rev. B* **98**, 174433 (2018).

[63] O. Sikora, F. Pollmann, N. Shannon, K. Penc, and P. Fulde, Quantum Liquid with Deconfined Fractional Excitations in Three Dimensions, *Phys. Rev. Lett.* **103**, 247001 (2009).

[64] P. W. Anderson, Ordering and antiferromagnetism in ferrites, *Phys. Rev.* **102**, 1008 (1956).

[65] D. S. Rokhsar and S. A. Kivelson, Superconductivity and the Quantum Hard-Core Dimer Gas, *Phys. Rev. Lett.* **61**, 2376 (1988).

[66] S. Balasubramanian, D. Bulmash, V. Galitski, and A. Vishwanath, Exact wavefunction dualities and phase diagrams of 3d quantum vertex models (2022).

[67] S. Balasubramanian, V. Galitski, and A. Vishwanath, Classical vertex model dualities in a family of two-dimensional frustrated quantum antiferromagnets, *Phys. Rev. B* **106**, 195127 (2022).

[68] L. Savary and L. Balents, Disorder-Induced Quantum Spin Liquid in Spin Ice Pyrochlores, *Phys. Rev. Lett.* **118**, 087203 (2017).

[69] C.-H. Chern, C.-N. Liao, and Y.-Z. Chou, Disorder from disorder and confinement in the quantum Ising model in the pyrochlore lattice, arXiv:1003.4204 [cond-mat] (2010).

[70] K. G. Wilson, Confinement of quarks, *Phys. Rev. D* **10**, 2445 (1974).

[71] A. M. Polyakov, Thermal Properties of Gauge fields and Quark Liberation (1978).

[72] J. B. Kogut, An introduction to lattice gauge theory and spin systems, *Rev. Mod. Phys.* **51**, 659 (1979).

[73] A. Celi, B. Vermersch, O. Viyuela, H. Pichler, M. D. Lukin, and P. Zoller, Emerging Two-Dimensional Gauge Theories in Rydberg Configurable Arrays, *Phys. Rev. X* **10**, 021057 (2020).

[74] J. Röchner, L. Balents, and K. P. Schmidt, Spin liquid and quantum phase transition without symmetry breaking in a frustrated three-dimensional ising model, *Phys. Rev. B* **94**, 201111 (2016).

[75] S. D. Pace, S. C. Morampudi, R. Moessner, and C. R. Laumann, Emergent Fine Structure Constant of Quantum Spin Ice Is Large, *Phys. Rev. Lett.* **127**, 117205 (2021).

[76] G. Chen, “Magnetic monopole” condensation of the pyrochlore ice $U(1)$ quantum spin liquid: Application to $\text{Pr}_2\text{Ir}_2\text{O}_7$ and $\text{Yb}_2\text{Ti}_2\text{O}_7$, *Phys. Rev. B* **94**, 205107 (2016).

[77] K. Slagle and Y. B. Kim, Fracton Topological Order from Nearest-Neighbor Two-Spin Interactions and Dualities, *Phys. Rev. B* **96**, 165106 (2017).

[78] R. G. Melko, B. C. den Hertog, and M. J. P. Gingras, Long-range order at low temperatures in dipolar spin ice, *Phys. Rev. Lett.* **87**, 067203 (2001).

[79] R. G. Melko and M. J. Gingras, Monte carlo studies of the dipolar spin ice model, *J. Condens. Matter Phys.*

16, R1277 (2004).

[80] L. Savary and L. Balents, Coulombic quantum liquids in spin-1/2 pyrochlores, Phys. Rev. Lett. **108**, 037202 (2012).

[81] R. Sahay, A. Vishwanath, and R. Verresen, Quantum spin puddles and lakes: Nisq-era spin liquids from non-equilibrium dynamics, arXiv preprint arXiv:2211.01381 (2022).

[82] W. H. Zurek, Cosmological experiments in superfluid helium?, Nature **317**, 505 (1985).

[83] T. W. Kibble, Topology of cosmic domains and strings, J. Phys. A **9**, 1387 (1976).

[84] A. Del Campo and W. H. Zurek, Universality of phase transition dynamics: Topological defects from symmetry breaking, Int. J. Mod. Phys. A **29**, 1430018 (2014).

[85] B. Svetitsky, Symmetry aspects of finite-temperature confinement transitions, Phys. Rep. **132**, 1 (1986).

[86] E. Fradkin, *Field theories of condensed matter physics* (Cambridge University Press, 2013).

[87] R. Shankar, *Quantum field theory and condensed matter: An introduction* (Cambridge University Press, 2017).

[88] K. Fredenhagen and M. Marcu, Charged states in Z_2 gauge theories, Commun. Math. Phys. **92**, 81 (1983).

[89] K. Fredenhagen and M. Marcu, Confinement criterion for qcd with dynamical quarks, Phys. Rev. Lett. **56**, 223 (1986).

[90] K. Fredenhagen and M. Marcu, Dual interpretation of order parameters for lattice gauge theories with matter fields, Nucl. Phys. B-Proceedings Supplements **4**, 352 (1988).

[91] M. Marcu, (uses of) an order parameter for lattice gauge theories with matter fields, in *Lattice Gauge Theory: A Challenge in Large-Scale Computing*, edited by B. Bunk, K. H. Müller, and K. Schilling (Springer US, Boston, MA, 1986) pp. 267–278.

[92] J. Bricmont and J. Frölich, An order parameter distinguishing between different phases of lattice gauge theories with matter fields, Phys. Lett. B **122**, 73 (1983).

[93] K. Gregor, D. A. Huse, R. Moessner, and S. L. Sondhi, Diagnosing deconfinement and topological order, New J. Phys. **13**, 025009 (2011).

[94] S. de Léséleuc, D. Barredo, V. Lienhard, A. Browaeys, and T. Lahaye, Optical control of the resonant dipole-dipole interaction between rydberg atoms, Phys. Rev. Lett. **119**, 053202 (2017).

[95] A. W. Glaetzle, M. Dalmonte, R. Nath, C. Gross, I. Bloch, and P. Zoller, Designing frustrated quantum magnets with laser-dressed rydberg atoms, Phys. Rev. Lett. **114**, 173002 (2015).

[96] R. M. W. van Bijnen and T. Pohl, Quantum magnetism and topological ordering via rydberg dressing near förster resonances, Phys. Rev. Lett. **114**, 243002 (2015).

[97] D. Petrosyan and K. Mølmer, Binding potentials and interaction gates between microwave-dressed rydberg atoms, Phys. Rev. Lett. **113**, 123003 (2014).

[98] T. Graß, P. Bienias, M. J. Gullans, R. Lundgren, J. Maciejko, and A. V. Gorshkov, Fractional quantum hall phases of bosons with tunable interactions: From the Laughlin liquid to a fractional wigner crystal, Phys. Rev. Lett. **121**, 253403 (2018).

[99] J. T. Young, P. Bienias, R. Belyansky, A. M. Kaufman, and A. V. Gorshkov, Asymmetric blockade and multi-qubit gates via dipole-dipole interactions, Phys. Rev. Lett. **127**, 120501 (2021).

[100] A. Lavasani, Z.-X. Luo, and S. Vijay, Monitored quantum dynamics and the kitaev spin liquid, arXiv preprint arXiv:2207.02877 (2022).

Appendix A: Gauge mean field theory

In this appendix, we first provide details of the gauge mean field theory calculation sketched in Sec. III B 1, with a focus on capturing the Higgs transition. Then, we attempt to use the same technique in the small- Ω limit to obtain the confinement-deconfinement transition. We find that, in this limit, the technique is fraught with a serious limitation stemming from neglecting gauge fluctuations.

Starting from Eq. (44) of Sec. III B 1 and performing the mean-field decoupling, we get

$$\begin{aligned} \hat{H}_{\text{MF}} &= \hat{H}_{\Phi} + \hat{H}_{\text{s}} + \hat{H}_{\text{c}}, \text{ where} \\ \hat{H}_{\Phi} &= \frac{V}{2} \sum_{\mathbf{r} \in A, B} \hat{Q}_{\mathbf{r}}^2 - \frac{\Omega}{2} \sum_{(\mathbf{r} \in A), \mu} \left(\hat{\Phi}_{\mathbf{r}}^{\dagger} \hat{\Phi}_{\mathbf{r} + \mathbf{e}_{\mu}} \langle \hat{s}_{\mathbf{r}, \mu}^+ \rangle + \text{H.c.} \right), \\ \hat{H}_{\text{s}} &= -\frac{\Omega}{2} \sum_{(\mathbf{r} \in A), \mu} \left(\langle \hat{\Phi}_{\mathbf{r}}^{\dagger} \hat{\Phi}_{\mathbf{r} + \mathbf{e}_{\mu}} \rangle \hat{s}_{\mathbf{r}, \mu}^+ + \text{H.c.} \right) \\ &\quad + \sum_{(\mathbf{r} \in A), \mu} \hat{s}_{\mathbf{r}, \mu}^z \sum_{(\mathbf{r}' \in A), \nu} (V_{\mu\nu}(\mathbf{r} - \mathbf{r}') \langle \hat{s}_{\mathbf{r}', \nu}^z \rangle), \\ \hat{H}_{\text{c}} &= \frac{\Omega}{2} \sum_{(\mathbf{r} \in A), \mu} \left(\langle \hat{\Phi}_{\mathbf{r}}^{\dagger} \hat{\Phi}_{\mathbf{r} + \mathbf{e}_{\mu}} \rangle \langle \hat{s}_{\mathbf{r}, \mu}^+ \rangle + \text{H.c.} \right) \\ &\quad - \frac{1}{2} \sum_{(\mathbf{r} \in A), \mu} \hat{s}_{\mathbf{r}, \mu}^z \sum_{(\mathbf{r}' \in A), \nu} (V_{\mu\nu}(\mathbf{r} - \mathbf{r}') \langle \hat{s}_{\mathbf{r}', \nu}^z \rangle). \end{aligned} \quad (\text{A1})$$

\hat{H}_{c} is a constant, and $V_{\mu\nu}(\mathbf{r} - \mathbf{r}')$ was defined in Sec. III B 1. \hat{H}_{s} above is of the form $-\sum_{(\mathbf{r} \in A), \mu} (h_{\mathbf{r}, \mu}^x \hat{s}_{\mathbf{r}, \mu}^x + h_{\mathbf{r}, \mu}^z \hat{s}_{\mathbf{r}, \mu}^z)$, where

$$\begin{aligned} h_{\mathbf{r}, \mu}^x &= \Omega \langle \hat{\Phi}_{\mathbf{r}}^{\dagger} \hat{\Phi}_{\mathbf{r} + \mathbf{e}_{\mu}} \rangle, \\ h_{\mathbf{r}, \mu}^z &= - \sum_{(\mathbf{r}' \in A), \nu} (V_{\mu\nu}(\mathbf{r} - \mathbf{r}') \langle \hat{s}_{\mathbf{r}', \nu}^z \rangle), \end{aligned} \quad (\text{A2})$$

and $\langle \hat{\Phi}_{\mathbf{r}}^{\dagger} \hat{\Phi}_{\mathbf{r} + \mathbf{e}_{\mu}} \rangle$ is calculated in the ground state of \hat{H}_{Φ} , which in turn depends on $\langle \hat{s}^+ \rangle$. (We have implicitly assumed here that $\langle \hat{\Phi}_{\mathbf{r}}^{\dagger} \hat{\Phi}_{\mathbf{r} + \mathbf{e}_{\mu}} \rangle$ is real, which we will show can be assumed self-consistently.) This implies that, in the ground state,

$$\langle \hat{s}_{\mathbf{r}, \mu}^i \rangle = \frac{h_{\mathbf{r}, \mu}^i}{2|\mathbf{h}_{\mathbf{r}, \mu}|} \text{ for } i = x, z. \quad (\text{A3})$$

Our goal is to self-consistently minimize the ground-state energy of the mean-field Hamiltonian subject to the constraints in Eqs. (42) and (43). We showed in Sec. III A 2 that the ordered ground state at $\Omega = 0$ has momentum

$\mathbf{k} = \mathbf{0}$. Also, the TFP state in the large- Ω limit is a $\mathbf{k} = \mathbf{0}$ state. So we start with a mean-field ansatz with full translation symmetry (similar to Ref. [80]):

$$\begin{aligned}\langle s_{\mathbf{r},\mu}^+ \rangle &= \frac{1}{2} \cos \theta, \\ \langle s_{\mathbf{r},\mu}^z \rangle &= \frac{1}{2} \varepsilon_\mu \sin \theta,\end{aligned}\quad (\text{A4})$$

where $\varepsilon_\mu = 1, 1, -1, -1$ for $\mu = 0, 1, 2, 3$, respectively. To solve the matter sector, it is convenient to deal with the Lagrangian instead of the Hamiltonian. The imaginary-time Lagrangian for the matter sector is

$$\begin{aligned}\mathcal{L} &= \frac{1}{2V} \sum_{\mathbf{r} \in A, B} |(\partial_\tau - iv_{\mathbf{r}})\Phi_{\mathbf{r}}|^2 \\ &\quad - \frac{\Omega \cos \theta}{4} \sum_{(\mathbf{r} \in A), \mu} (\Phi_{\mathbf{r}}^* \Phi_{\mathbf{r} + \mathbf{e}_\mu} e^{ia_{\mathbf{r},\mu}} + \text{c.c.}) \\ &\quad - i \sum_{\mathbf{r} \in A, B} \left[\eta_{\mathbf{r}} v_{\mathbf{r}} \left(\sum_\mu s_{\mathbf{r} + \eta_{\mathbf{r}} \mathbf{e}_\mu / 2}^z \right) + \tilde{\lambda}_{\mathbf{r}} (|\Phi_{\mathbf{r}}|^2 - 1) \right],\end{aligned}\quad (\text{A5})$$

where the Lagrange multiplier $\tilde{\lambda}_{\mathbf{r}}$ (which gets integrated over) enforces the constraint $|\Phi_{\mathbf{r}}|^2 = 1$. The Lagrange multiplier $v_{\mathbf{r}}$ enforces the constraint (43). To zeroth order, we ignore the gauge fluctuation $a_{\mathbf{r},\mu}$. The matter Lagrangian alone, despite being quadratic in the rotor variables, is nevertheless interacting because a quadratic term in rotor operators is nonlinear in terms of canonical bosons (in other words, it is a cosine term in the phase of the rotor.) In order to make progress, Ref. [80] assumes that, at the saddle point, $\tilde{\lambda}_{\mathbf{r}}$ takes on a spatially uniform and purely imaginary value $i\lambda$, and also implicitly assumes that $v_{\mathbf{r}}$ is 0 at the saddle point. Here, we will follow suit while acknowledging that these approximations are uncontrolled. Making these simplifications, we obtain

$$\begin{aligned}\mathcal{L} &= \frac{1}{2V} \sum_{\mathbf{r}} |\partial_\tau \Phi_{\mathbf{r}}|^2 - \frac{\Omega \cos \theta}{4} \sum_{(\mathbf{r} \in A), \mu} (\Phi_{\mathbf{r}}^* \Phi_{\mathbf{r} + \mathbf{e}_\mu} + \text{c.c.}) \\ &\quad + \lambda \sum_{\mathbf{r}} (|\Phi_{\mathbf{r}}|^2 - 1).\end{aligned}\quad (\text{A6})$$

The constraints now simplify to

$$\langle \Phi_{\mathbf{r}}^\dagger \Phi_{\mathbf{r}} \rangle = 1, \quad (\text{A7})$$

$$h^x = \Omega \langle \Phi_{\mathbf{r}}^\dagger \Phi_{\mathbf{r} + \mathbf{e}_\mu} \rangle. \quad (\text{A8})$$

Now, we have a quadratic Lagrangian, which we solve by Fourier transformation. Our Fourier transformation convention is (for $\alpha \in \{A, B\}$)

$$\Phi_{\mathbf{r},\alpha}(\tau) = T \sum_{\omega_n} \sum_{\mathbf{k} \in BZ} \Phi_{\mathbf{k},\alpha}(\omega_n) e^{i(\mathbf{k} \cdot \mathbf{r} - \omega_n \tau)}, \quad (\text{A9})$$

where T is the temperature, ω_n are Matsubara frequencies and we eventually take the limit $T \rightarrow 0$. Eq. (A6) becomes

$$\mathcal{L} = T \sum_{\mathbf{k}, \omega_n} (\Phi_{\mathbf{k},A}^*(\omega_n) \Phi_{\mathbf{k},B}^*(\omega_n)) \mathcal{G}_{\mathbf{k}}^{-1}(\omega_n) \begin{pmatrix} \Phi_{\mathbf{k},A}(\omega_n) \\ \Phi_{\mathbf{k},B}(\omega_n) \end{pmatrix}, \quad (\text{A10})$$

where

$$\mathcal{G}_{\mathbf{k}}^{-1}(\omega_n) = \begin{pmatrix} \frac{\omega_n^2}{2V} + \lambda & -\frac{\Omega \cos \theta}{4} f_{\mathbf{k}} \\ -\frac{\Omega \cos \theta}{4} f_{\mathbf{k}}^* & \frac{\omega_n^2}{2V} + \lambda \end{pmatrix}. \quad (\text{A11})$$

Here,

$$f_{\mathbf{k}} = 1 + e^{-ik_1} + e^{-ik_2} + e^{-ik_3}, \quad (\text{A12})$$

where $\mathbf{k} \equiv k_1 \mathbf{b}_1 + k_2 \mathbf{b}_2 + k_3 \mathbf{b}_3$, and $\mathbf{b}_1, \mathbf{b}_2$ and \mathbf{b}_3 are reciprocal lattice vectors of the FCC lattice satisfying $\mathbf{a}_i \cdot \mathbf{b}_j = \delta_{ij}$.

Upon inverting the above matrix, we find that the eigenvalues of $\mathcal{G}_{\mathbf{k}}(\omega_n)$ are $\frac{2V}{\omega_n^2 + (\omega_{\mathbf{k}}^{\pm}(\lambda, \theta))^2}$, where the dispersion of the two bosonic bands is

$$\omega_{\mathbf{k}}^{\pm}(\lambda, \theta) = \sqrt{2V \left(\lambda \pm \frac{\Omega \cos \theta}{4} |f_{\mathbf{k}}| \right)}. \quad (\text{A13})$$

As long as the spinon dispersion is gapped, spinons will not condense. From the dispersion above, we see that the dispersion becomes gapless when $\lambda = \Omega \cos \theta$. However, as we will see below, for fixed θ and Ω , λ is determined by the constraint in Eq. (A7). Therefore the condition $\lambda = \Omega \cos \theta$ is met for a specific $\Omega = \Omega_H^{\text{MF}}$, which we will calculate below. Before that, we will go through a few intermediate steps. First, the matrix form of $\mathcal{G}_{\mathbf{k}}(\omega_n)$ is (assuming $\Omega > 0$)

$$\mathcal{G}_{\mathbf{k}}(\omega_n) = V \begin{pmatrix} \frac{1}{\omega_n^2 + (\omega_{\mathbf{k}}^+)^2} + \frac{1}{\omega_n^2 + (\omega_{\mathbf{k}}^-)^2} & \mathbf{g}_{\mathbf{k}} \left(\frac{1}{\omega_n^2 + (\omega_{\mathbf{k}}^+)^2} - \frac{1}{\omega_n^2 + (\omega_{\mathbf{k}}^-)^2} \right) \\ \mathbf{g}_{\mathbf{k}}^* \left(\frac{1}{\omega_n^2 + (\omega_{\mathbf{k}}^+)^2} - \frac{1}{\omega_n^2 + (\omega_{\mathbf{k}}^-)^2} \right) & \frac{1}{\omega_n^2 + (\omega_{\mathbf{k}}^+)^2} + \frac{1}{\omega_n^2 + (\omega_{\mathbf{k}}^-)^2} \end{pmatrix}, \quad (\text{A14})$$

where

$$g_{\mathbf{k}} = \begin{cases} -\frac{f_{\mathbf{k}}}{|f_{\mathbf{k}}|} & \text{when } 0 \leq \theta < \pi/2, \\ 0 & \text{when } \theta = \pi/2. \end{cases} \quad (\text{A15})$$

With the Green's function in hand, we are now ready

to impose the constraints, Eq. (A7) and Eq. (A8). First, we calculate equal-time correlation functions of Φ (by performing the Matsubara sum on the Green's function). Using these, the constraints in Eq. (A7) and Eq. (A8) become, respectively,

$$F_1(\lambda, \theta) \equiv \frac{V}{2N_{\text{u.c.}}} \sum_{\mathbf{k}} \left(\frac{1}{|\omega_{\mathbf{k}}^+|} + \frac{1}{|\omega_{\mathbf{k}}^-|} \right) = 1, \quad (\text{A16})$$

$$\Omega F_2(\lambda, \theta) \equiv \Omega \frac{V}{2N_{\text{u.c.}}} \sum_{\mathbf{k}} g_{\mathbf{k}} \left(\frac{1}{|\omega_{\mathbf{k}}^-|} - \frac{1}{|\omega_{\mathbf{k}}^+|} \right) = h^x. \quad (\text{A17})$$

Next, by imposing Eq. (A3) with the help of Eq. (A2), we get

$$h^z = -\frac{\mathcal{B} \sin \theta}{2}, \text{ where } \mathcal{B} = \frac{\sin \theta}{2} \sum_{(\mathbf{r}' \in A), \nu} V_{0,\nu}(-\mathbf{r}') \varepsilon_{\nu}. \quad (\text{A18})$$

For a given θ , Eq. (A16) determines λ . We see that there are three self-consistent solutions for θ :

$$\theta = \begin{cases} 0, \\ \pi/2, \\ \cos^{-1} \left(\frac{2\Omega F_2(\lambda, \theta)}{\mathcal{B}} \right). \end{cases} \quad (\text{A19})$$

Within gMFT (gauge mean field theory), these three solutions correspond to a QSL, a ‘‘Coulomb ferromagnet’’ (spin liquid with nonzero ice ferromagnetic order parameter), and an ice ferromagnet, respectively [80]. For a fixed parameter Ω , the true solution depends on which of the three solutions above has lower energy with respect to the mean-field Hamiltonian (A1). Suppose that, for large enough Ω , one is in the QSL phase, i.e., $\theta = 0$ and $\langle \hat{\Phi}_{\mathbf{r}} \rangle = 0$. Now, the bosons will condense when their dispersion becomes gapless, i.e., $\lambda = \Omega$. Using constraint (A16), we find that this transition point is $\Omega_{\text{MF}}^H \approx 0.7V$, as also found in Ref. [68]. For $\Omega > \Omega_{\text{MF}}^H$, the ground state is in the TFP phase.

Having identified the Higgs transition point, we now attempt to identify the confinement-deconfinement transition for low Ω , i.e., find Ω at which $\theta = 0$ becomes the lowest-energy saddle-point. Using Eq. (A1), we get the following expression for the mean-field energy:

$$E_{\text{MF}} = K - N_{\text{u.c.}} \left(2\Omega F_2(\lambda, \theta) \cos \theta + \frac{\mathcal{B}}{2} \sin^2 \theta \right), \quad (\text{A20})$$

where K is the total kinetic energy of the bosons and can be calculated to be

$$K = \frac{1}{2} \sum_{\mathbf{k}} (\omega_{\mathbf{k}}^+ + \omega_{\mathbf{k}}^-). \quad (\text{A21})$$

In Fig. 16, we plot the energy E_{MF} for $\theta = 0$ (QSL) and $\theta = \pi/2$ (ice ferromagnet), and find a transition at $\Omega \approx 0.13V$. (The third solution for θ becomes the lowest-energy solution only in a minuscule window around $\Omega \approx$

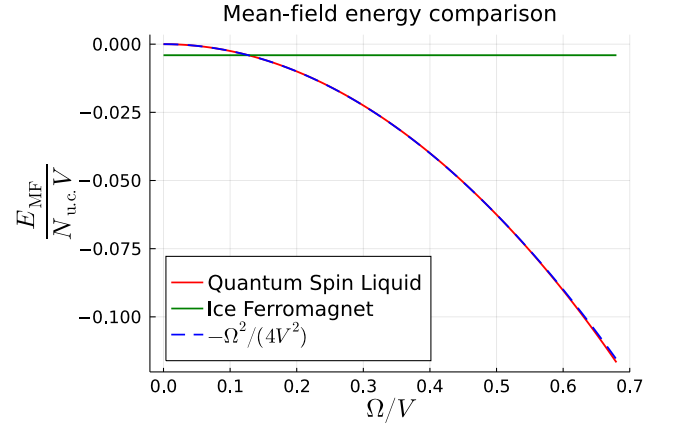


Figure 16: The energy per unit cell (in units of V) of saddle points $\theta = 0$ (QSL) and $\theta = \pi/2$ (ice ferromagnet) given by Eq. (A20) up to an overall additive constant that is the same for $\theta = 0$ and $\theta = \pi/2$. We also plot $-\frac{\Omega^2}{4V^2}$ arising from trivial spin-flip pairs: this plot almost overlaps with the energy of the $\theta = 0$ state.

0.13 V , so we ignore it.) However, we will now argue that this result is misleading.

In gMFT, the energy reduction in the QSL phase with respect to the ordered phase (ice ferromagnet) arises from the minimization of kinetic energy of the bosonic charges $\hat{\Phi}_{\mathbf{r}}$ that are allowed to hop. When $\theta = 0$, the hopping coefficient is maximized, while, for $\theta = \pi/2$, the hopping coefficient is 0. However, microscopically, this hopping corresponds to a single spin-flip. A pair of spin-flips at the same site leads to a *constant* reduction of energy coming from second order perturbation theory, given by $-\Omega^2 N_{\text{u.c.}}/V$. It is constant in the sense that this reduction is obtained for *any* state including the QSL and the ice ferromagnet. The mean-field calculation, however, unfairly assigns this reduction to the QSL but not to the ordered state. In fact, in Fig. 16, we have also plotted $-\Omega^2/(4V)$ (the factor of 1/4 can perhaps be attributed to using spin-1/2 and classical spins at the same time). As can be seen, this plot almost completely overlaps with the energy of the QSL calculated within gMFT. So it is clear that, within gMFT, the difference between the energies of the QSL and the confined phase is quadratic in Ω to leading order even though we know from perturbation theory that the leading order term should be proportional to Ω^6 . Hence, gMFT cannot be used in the vicinity of the confinement-deconfinement transition unless gauge-fluctuations are properly taken into consideration.

Appendix B: Corrections in the measurement protocol of the plaquette X correlator

In the protocol described in Sec. IV A 1, we equated the expectation value of $\prod_{i=1}^{12} (2\hat{S}_i^x)$ with $\hat{X}_P \hat{X}_{P'}$ in the ground state (more generally, the state prepared in ex-

periment) assuming that the state is supported entirely on the ice manifold. Corrections arise because this is satisfied only approximately. However, we show in this appendix that these corrections are of sixth order in Ω/V .

Let $|\Psi_g\rangle$ be the ground state of the system. This implies that $|\Psi_0\rangle = \hat{U}_S |\Psi_g\rangle$ is in the ice manifold, where \hat{U}_S is the unitary operator that implements the Schrieffer-Wolff transformation (see Sec. III A 1). First we show that the first order correction in Ω/V is zero in the limit $\Omega \ll V$.

The quantity measured in an experiment implementing the protocol of Sec. IV A 1, assuming that the experiment prepares the ground state, is

$$C_X^{\text{exp}} = \langle \Psi_g | e^{i\hat{H}_Y t_Y} \prod_{i=1}^{12} (2\hat{S}_i^z) e^{-i\hat{H}_Y t_Y} | \Psi_g \rangle \\ \approx \langle \Psi_0 | \hat{U}_S \hat{A} \hat{U}_S^\dagger | \Psi_0 \rangle,$$

where, $\hat{A} = \prod_{i=1}^{12} 2\hat{S}_i^x$. Now,

$$\hat{U}_S \hat{A} \hat{U}_S^\dagger = \hat{A} + [\hat{S}, \hat{A}] + \frac{1}{2!} [\hat{S}, [\hat{S}, \hat{A}]] \\ + \frac{1}{3!} [\hat{S}, [\hat{S}, [\hat{S}, \hat{A}]]] + \dots \quad (\text{B1})$$

Since $|\Psi_0\rangle$ is in the ice manifold, the expectation value of the first term above is the required plaquette X correlator, $\langle \Psi_0 | \hat{A} | \Psi_0 \rangle = \langle \Psi_0 | \hat{X}_P \hat{X}_{P'} | \Psi_0 \rangle$, as explained in Sec. IV A 1. The expectation value of the remaining terms is the error. \hat{S} can be written as $\sum_{i=1}^{\infty} \hat{S}_i$ where \hat{S}_i is of order $(\Omega/V)^i$. First, we will show that the first order error, $\mathcal{E}_1 = \langle \Psi_0 | [\hat{S}_1, \hat{A}] | \Psi_0 \rangle$, is zero using the expressions for \hat{S} up to first order in Ω/V from Appendix B of [40]:

$$\hat{S}_1 = \hat{\mathcal{P}} \hat{H}_\Omega \hat{\mathcal{D}} - \hat{\mathcal{D}} \hat{H}_\Omega \hat{\mathcal{P}}, \text{ where } \hat{\mathcal{D}} = -\frac{\hat{1} - \hat{\mathcal{P}}}{\hat{H}_0 - E_0}. \quad (\text{B2})$$

Here, $\hat{\mathcal{P}}$ is the projector into the ice manifold, E_0 is the energy of the ice manifold, and \hat{H}_0 and \hat{H}_Ω are given in Eq. (6). Plugging in the expression for \hat{S}_1 in \mathcal{E}_1 gives

$$\mathcal{E}_1 = \langle \hat{\mathcal{P}} \hat{H}_\Omega \hat{\mathcal{D}} \hat{A} - \hat{A} \hat{\mathcal{P}} \hat{H}_\Omega \hat{\mathcal{D}} - \hat{\mathcal{D}} \hat{H}_\Omega \hat{\mathcal{P}} \hat{A} + \hat{A} \hat{\mathcal{D}} \hat{H}_\Omega \hat{\mathcal{P}} \rangle_0 \\ = \langle \Psi_0 | \hat{H}_\Omega \hat{\mathcal{D}} \hat{A} | \Psi_0 \rangle + \langle \Psi_0 | \hat{A} \hat{\mathcal{D}} \hat{H}_\Omega | \Psi_0 \rangle. \quad (\text{B3})$$

We have used $\hat{\mathcal{D}} | \Psi_0 \rangle = 0$ and $\hat{\mathcal{P}} | \Psi_0 \rangle = | \Psi_0 \rangle$ above, and the expectation values are taken in $|\Psi_0\rangle$. Since \hat{A} flips the 12 spins on P and P' , while \hat{H}_Ω flips only one spin, it is not possible to go back to the ice manifold after applying $\hat{H}_\Omega \hat{\mathcal{D}} \hat{A}$ on $|\Psi_0\rangle$. Thus $\langle \hat{H}_\Omega \hat{\mathcal{D}} \hat{A} \rangle_0 = 0$, implying $\mathcal{E}_1 = 0$.

The corrections at order i involves expectation value in $|\Psi_0\rangle$ of operators that consist of i factors of \hat{H}_Ω and one factor of \hat{A} . For example, the second-order error is

$$\mathcal{E}_2 = \langle \Psi_0 | [\hat{S}_2, \hat{A}] + \frac{1}{2!} [\hat{S}_1, [\hat{S}_1, \hat{A}]] | \Psi_0 \rangle, \quad (\text{B4})$$

where

$$\hat{S}_2 = \hat{\mathcal{P}} \hat{H}_\Omega \hat{\mathcal{D}} \hat{H}_\Omega \hat{\mathcal{D}} - \hat{\mathcal{D}} \hat{H}_\Omega \hat{\mathcal{D}} \hat{H}_\Omega \hat{\mathcal{P}} - \hat{\mathcal{P}} \hat{H}_\Omega \hat{\mathcal{P}} \hat{H}_\Omega \hat{\mathcal{D}}^2 \\ + \hat{\mathcal{D}}^2 \hat{H}_\Omega \hat{\mathcal{P}} \hat{H}_\Omega \hat{\mathcal{P}}. \quad (\text{B5})$$

It can be seen that, at order $i = 1, 2, 3, 4$, and 5 , the error will be zero because \hat{A} would flip 12 spins, while i factors of \hat{H}_Ω would flip only i spins. At sixth order, however, the error can be nonzero if $|\Psi_0\rangle$ has support on a configuration where one of the two plaquettes, say P' , is flippable. In such a situation, \hat{A} will map P' to the complementary flippable configuration and will also flip the spins on P . The six factors of \hat{H}_Ω can bring P back to the original configuration, giving a state within the ice manifold which could have nonzero overlap with $|\Psi_0\rangle$.

In conclusion, we find that the experimentally measured correlator, C_X^{exp} , is the same as the theoretically needed correlator, $\langle \Psi_0 | \hat{X}_P \hat{X}_{P'} | \Psi_0 \rangle$, with corrections of order $(\Omega/V)^6$:

$$C_X^{\text{exp}} = \langle \Psi_0 | \hat{X}_P \hat{X}_{P'} | \Psi_0 \rangle + \Theta((\Omega/V)^6). \quad (\text{B6})$$